JGR Solid Earth

RESEARCH ARTICLE
10.1029/2023JB026458

# Grain-Size Effects During Semi-Brittle Flow of Calcite Rocks

**Christopher Harbord[1], Nicolas Brantut[1], and David Wallis[2]**

[1]Department of Earth Sciences, University College London, London, UK, [2]Department of Earth Sciences, University of Cambridge, Cambridge, UK

**Key Points:**

- Flow stress of calcite rocks scales with the inverse of grain size to a power between 1/3 and 2/3
- Hardening rate approximately doubles from coarse-grained (2 mm) to fine-grained (10 μm) samples
- Twin spacing exerts a weaker control than grain size on strength

**Correspondence to:**

N. Brantut,
n.brantut@ucl.ac.uk

**Citation:**

Harbord, C., Brantut, N., & Wallis, D. (2023). Grain-size effects during semi-brittle flow of calcite rocks. *Journal of Geophysical Research: Solid Earth*, *128*, e2023JB026458. https://doi.org/10.1029/2023JB026458

Received 2 FEB 2023
Accepted 14 JUL 2023



**Abstract** We study the role of grain size in the rheological behavior of calcite aggregates in the semi-brittle regime. We conduct compressive triaxial deformation tests on three rocks, Solnhofen limestone, Carrara marble and Wombeyan marble, with grain sizes of 5–10, 200, and 2 mm, respectively, at pressures in the range 200–800 MPa and temperatures in the range 20–400°C. At all conditions, both strength and hardening rate increase with decreasing grain size. Flow stress scales with the inverse of grain size to a power between 1/3 and 2/3. For a given pressure and temperature, the typical strength of Solnhofen limestone (grain size 5–10 μm), is greater than that of Wombeyan marble, (grain size of around 2 mm), by about 200–300 MPa (i.e., around a factor of 2). Hardening rate decreases linearly with the logarithm of grain size. In situ ultrasonic monitoring reveals that *P*-wave speed tends to decrease with increasing strain, and that this decrease is more marked at room temperature than at 200 and 400°C. The decrease in wave speed is consistent with microcracking, which is more prevalent at low temperature and low pressure. Microstructural observations reveal high twin densities in all deformed samples. Twin density increases with stress, consistent with previous datasets. Spatial distributions of intragranular misorientation indicate that twins are sometimes obstacles to dislocation motion, but this effect is not ubiquitous. Computed slip-transfer statistics indicate that twins are typically weaker barriers to dislocation glide than grain boundaries, so that their effect on dislocation accumulation and hardening rates is likely smaller than the effect of grain size.

**Plain Language Summary** Rocks are strongest when their failure mode is mixed between brittle (fracture processes) and crystal plastic (individual grains deform by movement of crystal defects). Unfortunately, we have a limited understanding of how these two mechanisms accommodate deformation together. Yet, both failure modes are sensitive to grain size. We selected three calcite rocks of varying grain size and deformed them at elevated pressure and temperature to simulate coupled brittle and crystal-plastic deformation. Calcite also forms twins (small planar structures in the crystal) when deformed that may act to strengthen the rock during deformation. By monitoring the speed at which sound waves pass through the rock during experiments, we were able to track brittle behavior. We find that smaller grain size results in greater strength. We observe twins in all deformed samples, but they do not seem to have a big effect on the resulting strength. Microscopic observations of samples and wave-speed measurements show that brittle behavior is restricted by increases in pressure and temperature. We suggest a new approach to model these processes that could be used to model coupled brittle and crystal-plastic behavior on a large scale.

## 1. Introduction

In the shallow lithosphere, rocks deform by localized brittle failure and strength is described by a friction law (Scholz, 2002; Townend & Zoback, 2000). In the lower lithosphere, high temperatures and pressures promote the onset of crystal-plastic deformation mechanisms. Here, strength is described by flow laws sensitive to temperature ($T$) and strain rate ($\dot{\varepsilon}$) (Evans & Kohlstedt, 1995; Goetze & Brace, 1972). At intermediate conditions, deformation is ductile, that is, remains macroscopically distributed (following the terminology of Rutter (1986)), and is often termed "semi-brittle," which is characterized by coupled cracking and crystal plasticity. Semi-brittle deformation is likely to support the highest stresses in the lithosphere (Brace & Kohlstedt, 1980; Goetze & Evans, 1979), impacting geodynamic processes (Burov, 2011) and the maximum depth of earthquake nucleation (Scholz, 1998). Despite the significance of semi-brittle flow, there is a paucity of simple models to describe the rheological behavior of rock in this regime, and the relative importance of key processes, such as friction, tensile cracking, dislocation motion, twinning, or grain-boundary sliding is not well constrained. Thus, to advance our understanding of semi-brittle flow, we must first improve our understanding of interactions among microscale deformation processes.

Calcite rock is an important constituent of tectonic terrains, and undergoes a transition to semi-brittle flow at modest pressure and low temperature (e.g., Fredrich et al., 1989; Heard, 1960). This combination of characteristics has led to numerous laboratory investigations into the rheological behavior of calcite rock across the brittle-ductile transition (see Rybacki et al. (2021) and references therein). The main deformation behaviors of calcite rock can be illustrated using the case of Carrara marble, a relatively isotropic, pure calcite aggregate with little initial crack porosity and equant grain shapes with sizes in the range 60–200 μm. At room temperature, Carrara marble is dilatant and brittle at low pressure ($P < 30$ MPa), and its strength is controlled by friction. At intermediate pressures ($30 < P < 300$ MPa), calcite rocks deform in a semi-brittle manner, and strength becomes decreasingly pressure sensitive with increasing pressure (Fredrich et al., 1989). When pressure is high enough ($P > 300$ MPa), strength becomes independent of confining pressure and deformation is nondilatant (Edmond & Paterson, 1972). Furthermore, increases in temperature reduce the pressure required to promote semi-brittle flow (Rybacki et al., 2021). Edmond and Paterson (1972) and Fischer and Paterson (1989) report in situ changes of volumetric strain during deformation of calcite rocks, finding that dilatancy is reduced by increasing pressure. Furthermore, sample volume remains constant when strength is independent of pressure (Edmond & Paterson, 1972). More recently, Schubnel et al. (2005) and Rybacki et al. (2021) measured in situ *P*-wave velocity ($V_p$) and demonstrated that wave-speed decreases during deformation are suppressed by pressure increases. In situ measurements therefore support microstructural observations in implying that increasing pressure limits cracking and frictional sliding whilst promoting crystal-plastic processes.

Microstructural observations from calcite rocks deformed in the semi-brittle regime reveal that distributed cracking, twinning, and dislocation motion act together to accommodate strain (Fredrich et al., 1989). *Post-mortem* crack density decreases with increasing confining pressure (Fredrich et al., 1989), approaching zero when strength is independent of confining pressure. Additionally, deformation twins are present in calcite rocks deformed at conditions below 800°C (Rybacki et al., 2021), and twin spacing depends on stress (Rowe & Rutter, 1990). Detailed strain measurements at the grain scale reveal that twinning occurs readily in well oriented grains (those with high Schmid factor for twinning), and that it is likely associated with a local backstress that causes hardening of twinned grains (Spiers, 1979). In addition, microscale strain mapping also indicates the existence of shear localized along grain boundaries at temperatures <800°C, potentially identifying grain-boundary sliding as a possible deformation mechanism (Quintanilla-Terminel et al., 2017).

Another common rheological behavior of semi-brittle flow in calcite rocks is strain hardening, which can persist to high temperatures (<800°C, see Rybacki et al., 2021). At low temperature, strain hardening can arise from microscopic frictional slip across distributed defects, such as grain boundaries (e.g., David et al., 2020). In dislocation-mediated deformation regimes, strain hardening occurs due to an increase in dislocation density caused by inefficient recovery mechanisms (e.g., lack of dislocation climb) (Mecking & Kocks, 1981) and is sensitive to microstructure. In particular, grain boundaries can act as barriers to dislocation motion, resulting in increases in strength and sometimes increases in hardening rates with decreasing grain size for most metals (grain-size strengthening, see Cordero et al., 2016), and some geological materials (e.g., olivine, Hansen et al., 2019). Alternatively, strain hardening in calcite rocks has been proposed to be enhanced by twinning (Rybacki et al., 2021). Twins may not contribute significantly to the total strain, but they could indirectly enhance strength and hardening by providing additional barriers to dislocations. Indeed, transmission electron microscopy observations show that dislocation densities are elevated adjacent to twin boundaries (Barber & Wenk, 1979; Fredrich et al., 1989; Rybacki et al., 2021). In the metallurgy literature (De Cooman et al., 2018), the additional hardening provided by twins is commonly known as twinning-induced plasticity, or TWIP. TWIP originates from observations of high-manganese steels, where high hardening rates and ductility occur as a result of the formation of deformation twins (De Cooman et al., 2018). The hardening rates in these metals are attributed to a "dynamic Hall-Petch effect" in which twinning refines the intracrystalline microstructure and thereby reduces the dislocation mean free path. In this case, twin spacing exerts a significant control on strength and hardening and thereby limits sensitivity to grain size.

The semi-brittle regime in calcite rock is thus characterized by many interacting deformation mechanisms. One way to quantify the relative contribution of each mechanism to the overall rheological behavior is to test the impact of independent variables beyond the usual pressure and temperature conditions and imposed strain rate. One such variable is the grain size. At room temperature, yield stress ($\sigma_y$) and the transition pressure to semi-brittle deformation increase with decreasing grain size (Fredrich et al., 1990; Olsson, 1974). Grain size also impacts the strength of marble tested at elevated temperature in the dislocation-creep regime, which could be

**Table 1**
*Composition and Physical Properties of Starting Materials*

| | Solnhofen limestone | Carrara marble | Wombeyan marble |
|---|---|---|---|
| Abbreviation | SL | CM | WM |
| Composition | >99% $CaCO_3$ | >99% $CaCO_3$ | 96% $CaCO_3$ 2.5% $MgCO_3$ |
| Porosity (%) | 4% | <0.5% | <0.5% |
| $D$ (mm) | 0.005–0.01 | 0.06–0.22 | 1–2 |
| Initial $V_p$ (m $s^{-1}$) | 5,600 | 5,900 | – |

consistent with a Hall-Petch effect (Renner et al., 2002). In the high-pressure, moderate-temperature range ($P$ > 200 MPa, $T$ < 400°C) where twinning is ubiquitous, models of twinning-induced plasticity suggest that twin density rather than grain size is the main control on strength (Rybacki et al., 2021). To test this hypothesis, here we explore the role of grain size in semi-brittle rheological behavior and the brittle-plastic transition in calcite rocks for comparison to the role of twin density.

We performed a series of experiments at a range of pressures ($P \leq$ 800 MPa) and temperatures (≤400°C) using calcite rocks spanning two orders of magnitude in grain size: Solnhofen limestone (grain size less than 10 μm), Carrara marble (grain size on the order of 100 μm), and Wombeyan marble (grain size on the order of 1 mm). Experiments are supplemented by in situ measurements of axis-parallel *P*-wave speed and *post-mortem* microstructural investigations to infer deformation mechanisms. We find that grain size has a significant impact on both strength and hardening rate, and that the influence of twins is not as strong as would be expected from dynamic Hall-Petch models of TWIP hardening (Bouaziz et al., 2008).

## 2. Methods

### 2.1. Sample Materials

Three calcite rocks were selected for experiments, with grain size, $D$, spanning three orders of magnitude. Here we define grain size as the diameter of grains measured using the linear intercept method. Solnhofen limestone is a lithographic limestone with equant grains of size 5–10 μm (French et al., 2022), composed of >99.9% calcite, and with an initial porosity (measured with helium pycnometry) of 4% (Baud et al., 2000). Carrara Marble is a medium-grained marble with equant grains of size 60–220 μm, comprised of >99.9% calcite with a porosity of <0.1%. In the starting material, most grains exhibit at least one twin set. Wombeyan marble is a coarse-grained marble with a grain size of 1–2 mm, comprised of 96% calcite. Grains are equant and typically twinned in at least one plane, with an initial twin density of 60 $mm^{-1}$. This material was obtained thanks to Ian Jackson at the Australian National University, and is the same rock that was used by Paterson (1958). See Table 1 for further petrographic details.

### 2.2. Mechanical Testing

A total of 42 experiments were conducted in the "Murrell" gas-medium triaxial apparatus hosted at University College London (Harbord et al., 2022). Rectified cores, 10 mm in diameter and 22 mm in length, were dried in an oven at 70°C for at least 24 hr before testing. Samples were inserted into annealed copper jackets of 0.1 mm wall thickness and were swaged onto the deformation rams using a slip ring (Figure 1a). The jacketed samples were inserted into the pressure vessel and pressurized to the target confining pressure using argon gas. Here the confining pressure provides the equal subsidiary principal stresses. Throughout the tests, the measured pressure remained within 5% of the target pressure. An internal furnace was used to heat samples to 200 and 400°C. Axial load was applied parallel to the sample axis, generating the differential stress, $\sigma$. Axial stress was measured by an external load cell, and axial shortening was measured by a pair of linear variable-displacement transducers. Axial deformation was then applied by a piston that moved at a constant imposed shortening rate of 0.22 μm $s^{-1}$, equivalent to a strain rate of $10^{-5}$ $s^{-1}$. All samples were deformed to a total strain of 7.5%. A detailed list of test conditions is given in Table 3.

### 2.3. Data Processing

Several corrections were made to the mechanical data. Seal friction and jacket strength were subtracted from load measurements (as reported in Harbord et al. (2022)) and displacement due to machine compliance was subtracted from shortening measurements. The differential stress supported by the sample was computed by dividing the corrected force by the cross-sectional area of the sample, which was assumed to linearly increase with deformation consistent with a constant sample volume. Mechanical data were then further processed to obtain estimates

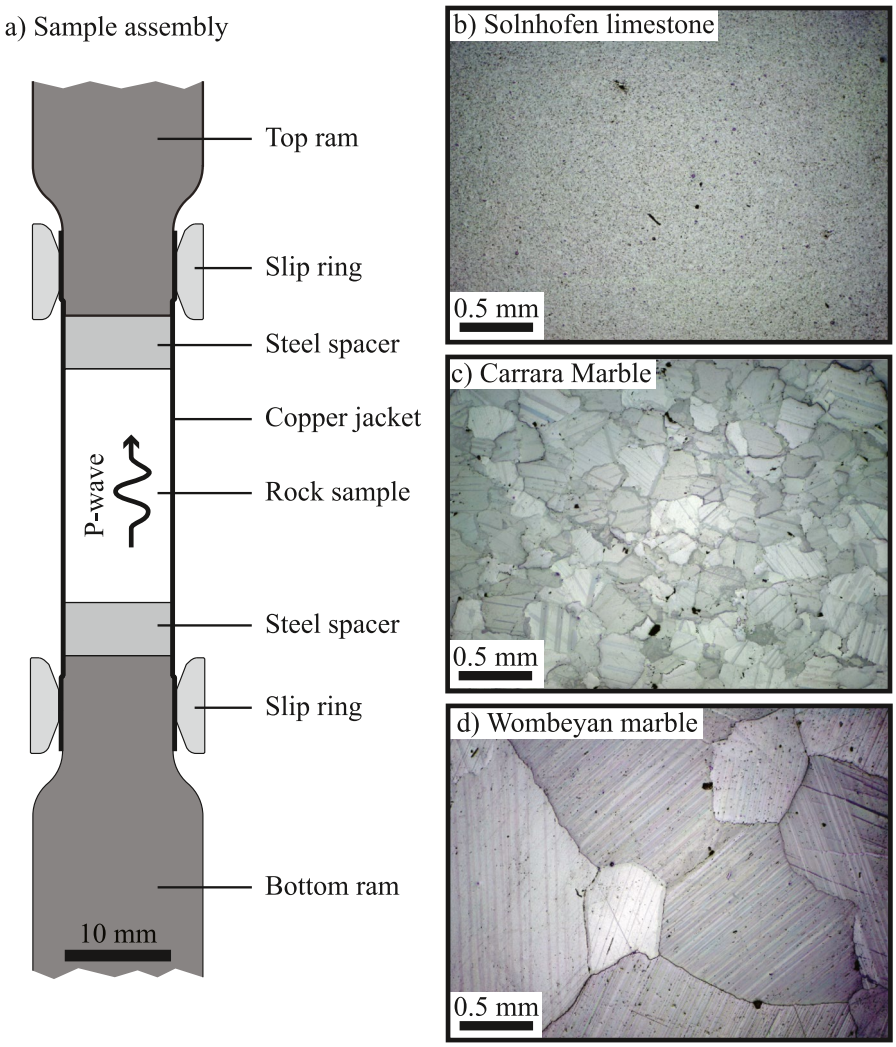


**Figure 1.** (a) Detail of sample geometry in the pressure vessel. Insets (b–d): Polarized incident-light images of initial sample microstructure of (b) Solnhofen limestone, (c) Carrara marble, and (d) Wombeyan marble. $V_p$ is defined as the longitudinal *P*-wave speed.

of the tangent modulus ($h = \delta\sigma/\delta\varepsilon$) by numerical differentiation of the stress data over a moving window of 1% strain. Uncertainties in seal friction during deformation result in error on the hardening modulus that is <20% of reported values. The yield stress ($\sigma_y$) is defined as the stress at which $h$ falls to 90% of the sample-specific Young's modulus determined from elastic loading.

### 2.4. In Situ *P*-Wave Speed Measurements

In situ *P*-wave speed was measured during tests conducted on Solnhofen limestone and Carrara marble. Measurements were made parallel to the sample axis during deformation using the pulse-transmission method (Birch, 1961). Every 10 s during the experiments, a 200 V pulse of 0.4 μs duration and 2.5 MHz frequency was sent to a lead-titanate-zirconate (PZT) ceramic disk mounted centrally in the bottom ram, which was received by a transducer mounted centrally at the top of the sample assembly and recorded digitally at 100 MHz (see Harbord et al., 2022, for further details). The lower PZT disk is positioned approximately 100 mm from the base of the sample and the upper disk is approximately 130 mm above the sample acoustic pulses traverse four separate interfaces comprising two sample-spacer piston interfaces and two sample sample-spacer interfaces (Figure 1). The signal-to-noise ratio was improved by stacking 256 raw traces at each time interval. Changes in axial *P*-wave speed were computed relative to a reference waveform using cross correlation, and corrected for interfacial delays

**Table 2**
*EBSD Acquisition Parameters for Each Map*

| Figures | Expt. | Lithology | Step (μm) | Map (X × Y) | EBSP pixels (X × Y) |
|---|---|---|---|---|---|
| Figure 11a | Run0119 | WM | 15 | 480 × 110 | 622 × 512 |
| Figure 11b | Run0093 | CM | 2 | 479 × 359 | 622 × 512 |
| Figure 11c | Run0167 | SL | 0.15 | 250 × 191 | 622 × 512 |
| Figure 12a | Run0093 | CM | 2 | 479 × 359 | 622 × 512 |
| Figure 12b | Run0093 | CM | 0.5 | 450 × 470 | 622 × 512 |
| Figure 12c | Run0093 | CM | 0.5 | 340 × 285 | 622 × 512 |
| Figure 12d | Run0093 | CM | 0.5 | 560 × 560 | 622 × 512 |
| Figure 13a | Run0093 | CM | 0.2 | 260 × 175 | 1,244 × 1,024 |
| Figure 13b | Run0093 | CM | 0.15 | 300 × 130 | 1,244 × 1,024 |

*Note.* WM is Wombeyan Marble, CM is Carrara Marble, SL is Solnhofen limestone and EBSP is electron backscatter pattern.

following the methods outlined in Harbord et al. (2022). Measurements of *P*-wave speed are reported as the change of wave speed ($\Delta V$) and are normalized relative to the wave speed measured at the start of loading ($V_0$). Selected deformation tests were subsequently repeated, and wave-speed changes were found to be reproducible.

To gain insight into the microstructural state of samples after deformation during the return to ambient pressure, we continued to perform wave-speed surveys after removal of differential stress and throughout the staged decompression. The change in wave speed during decompression is quantified as the relative change in wave speed ($\Delta V$) normalized by the wave speed measured at the end of deformation ($V_{final}$), and when at temperature, after cooling of the sample. These measurements were also complemented by *post-mortem* measurements of wave speed at room pressure (0.1 MPa) use a separate bench-top apparatus.

## 2.5. Microstructural Analysis

### 2.5.1. Optical Microscopy

To investigate deformation microstructures, selected samples were mounted in epoxy, sectioned parallel to the deformation axis, and polished. A set of thin sections was also made for visible-light microscope observations. Imaging using transmitted and reflected light was performed using a Leica DM750P microscope furnished with an ICC50 camera. To quantify the prevalence of intragranular cracks in each sample, we followed the method outlined by Fredrich et al. (1989). Samples were imaged using reflected light at ×4 magnification, and we counted intersections between cracks (excluding grain boundaries) and a square grid of 2 mm by 2 mm with a spacing of 0.2 mm. These counts were used to determine the resulting crack surface area per volume, $S_v$ ($mm^2/mm^3$).

### 2.5.2. Electron Microscopy

Scanning electron microscopy was performed using a Jeol JSM-6480LV scanning electron microscope (SEM) hosted at University College London and a Zeiss Gemini 300 field-emission gun SEM at the University of Cambridge. Electron backscatter diffraction (EBSD) patterns and forescattered electron images were collected using an Oxford Instruments Symmetry detector and AZtec 4.0 acquisition software. Table 2 lists the acquisition parameters for each EBSD data set. All diffraction patterns with acquired with low detector gain. Datasets collected for conventional EBSD were acquired with a reduced number of pixels in the diffraction patterns to increase the mapping speed. Datasets collected for high-angular resolution electron backscatter diffraction (HR-EBSD) were collected with the maximum number of pixels permitted by the detector.

HR-EBSD is a postprocessing technique that analyses distortion of the diffraction patterns to measure lattice rotations and intragranular heterogeneity in elastic strain (Britton & Wilkinson, 2011, 2012; Wilkinson et al., 2006). Full details of the technique are given by Wallis et al. (2019) and here we provide a summary of the key points. One diffraction pattern from the host grain within each mapped area was manually selected to be a reference pattern based on the quality of the diffraction pattern and its position within the map. 100 regions of interest, 256 × 256 pixels in size, were extracted from all diffraction patterns within the host grain. Each region of interest from each diffraction pattern was cross-correlated with the corresponding region of interest from the reference pattern to determine shifts in their positions. Shifts in the diffraction pattern due to beam scanning were corrected using a calibration determined on an undeformed Si single crystal following Wilkinson et al. (2006) and the position of the pattern center was calibrated using diffraction patterns collected over a range of detector insertion distances (Maurice et al., 2011). A deformation-gradient tensor was fit to the field of shifts in each diffraction pattern. The deformation-gradient tensor was decomposed into its symmetric and antisymmetric parts, which respectively give the elastic-strain and rotation tensors (Wilkinson et al., 2006). We used the pattern remapping approach of Britton and Wilkinson (2012), in which a first pass of cross-correlation measures lattice rotations that are used to rotate each pattern back into the orientation of the reference pattern before a second pass of cross-correlation measures the elastic strain and a small correction to the rotations. The elastic strains were converted to stresses using Hooke's law. The measured stresses are relative to the unknown stress state at the reference point, giving maps of intragranular stress heterogeneity, rather than absolute values. We subtracted the arithmetic mean value of each component of the stress tensor within the map area from each measured value so that the final maps provide

**Table 3**
*Table of Experiments Conducted at a Range of Conditions*

| Experiment | Lithology | $P$ (MPa) | $T$ (°C) | $\sigma_5$ (MPa) | $h_5$ (GPa) |
|---|---|---|---|---|---|
| Run0147* | Solnhofen limestone | 207 | 20.1 | 466 | 0.34 |
| Run0149* | Solnhofen limestone | 416 | 20.4 | 535 | 1.57 |
| Run0150* | Solnhofen limestone | 628 | 19.8 | 517 | 1.85 |
| Run0152* | Solnhofen limestone | 225 | 195 | 437 | 1.25 |
| Run0153* | Solnhofen limestone | 440 | 180 | 474 | 2.22 |
| Run0154* | Solnhofen limestone | 217 | 393 | 436 | 1.36 |
| Run0162* | Solnhofen limestone | 435 | 394 | 456 | 1.56 |
| Run0167* | Solnhofen limestone | 610 | 186 | 474 | 2.54 |
| Run0168* | Solnhofen limestone | 617 | 398 | 416 | 1.84 |
| Run0075 | Carrara marble | 200 | 19.8 | 344 | 1.22 |
| Run0078 | Carrara marble | 405 | 19.8 | – | – |
| Run0084 | Carrara marble | 615 | 19.8 | 386 | 1.83 |
| Run0086 | Carrara marble | 236 | 197 | 187 | 0.73 |
| Run0089 | Carrara marble | 366 | 204 | 272 | 1.91 |
| Run0090 | Carrara marble | 213 | 390 | 203 | 0.82 |
| Run0091 | Carrara marble | 378 | 405 | 186 | 0.72 |
| Run0093 | Carrara marble | 599 | 192 | 295 | 1.37 |
| Run0094 | Carrara marble | 594 | 401 | 198 | 0.65 |
| Run0095 | Carrara marble | 602 | 206 | – | – |
| Run0097 | Carrara marble | 597 | 204 | – | – |
| Run0098 | Carrara marble | 769 | 20.1 | 377 | 1.67 |
| Run0129* | Carrara marble | 403 | 17.6 | 385 | 1.67 |
| Run0131* | Carrara marble | 202 | 18.1 | 335 | 1.12 |
| Run0132* | Carrara marble | 407 | 18.2 | 354 | 1.31 |
| Run0137* | Carrara marble | 556 | 19.1 | 378 | 1.73 |
| Run0138* | Carrara marble | 220 | 172 | 267 | 1.41 |
| Run0141* | Carrara marble | 241 | 387 | 221 | 1.22 |
| Run0143* | Carrara marble | 579 | 20.2 | 376 | 1.63 |
| Run0145* | Carrara marble | 417 | 370 | 222 | 0.93 |
| Run0163* | Carrara marble | 616 | 171 | 247 | 1.58 |
| Run0164* | Carrara marble | 622 | 368 | 255 | 1.28 |
| Run0165* | Carrara marble | 391 | 195 | 321 | 2.17 |
| Run0166* | Carrara marble | 188 | 183 | 306 | 1.71 |
| Run0169* | Carrara marble | 203 | 16.3 | 341 | 1.36 |
| Run0104 | Wombeyan marble | 206 | 19.3 | 279 | 0.76 |
| Run0106 | Wombeyan marble | 594 | 20.2 | 330 | 1.15 |
| Run0110 | Wombeyan marble | 231 | 207 | 189 | 1.19 |
| Run0119 | Wombeyan marble | 609 | 187 | 218 | 0.55 |
| Run0120 | Wombeyan marble | 408 | 19.2 | 338 | 0.75 |
| Run0121 | Wombeyan marble | 428 | 190 | 226 | 0.71 |
| Run0124 | Wombeyan marble | 233 | 408 | 128 | 0.08 |

stress heterogeneity relative to the unknown mean stress state within each grain (Mikami et al., 2015). Alongside, spatial gradients in the lattice rotations were used to estimate densities of geometrically necessary dislocations (GNDs). Densities of each dislocation type on the slip systems summarized by J. H. De Bresser and Spiers (1997) were fit to the measurable components of the lattice curvature following the approach applied to quartz by Wallis et al. (2019). We emphasize that the stress heterogeneity and GND densities are determined independently, being respectively derived from the distinct symmetric and antisymmetric parts of the deformation-gradient tensor. Data points were filtered out if they had a mean normalized peak height in the cross-correlation function of <0.3 or a mean angular error in the fitted deformation gradient tensor of >0.004 radians (Britton & Wilkinson, 2011).

We analyzed the probability distributions of the stress heterogeneity to assess whether the stresses are imparted by dislocations. The probability distribution of the stress field of population of dislocations has a characteristic form with tails that depart from a normal distribution toward higher stresses (Jiang et al., 2013; Wilkinson et al., 2014). We assess for the presence of these tails using a normal-probability plot, in which the cumulative-probability axis is scaled such that a normal distribution falls on a straight line. Importantly, the tails of the probability distribution, $P(\sigma)$, have a specific form if the stresses, $\sigma$, are imparted by dislocations, whereby $P(\sigma) \rightarrow C\rho|\sigma|^{-3}$, where $C$ is a constant that depends on the material, type(s) of dislocation, and considered stress component, and $\rho$ is the total dislocation density (Groma & Bakó, 1998; Wilkinson et al., 2014). To test whether the measured stress fields exhibit this form, we compute the restricted second moment, $\nu_2$, which is a metric that characterizes the shape of a probability distribution based on the integral over restricted ranges in stress, calculated as $\nu_2(\sigma) = \int_{-\sigma}^{+\sigma} P(\sigma)\sigma^2 \, d\sigma$ (Kalácska et al., 2017; Wilkinson et al., 2014). A plot of $\nu_2$ versus $\ln(\sigma)$ becomes a straight line at high stresses if the tails of the probability distribution of the stresses exhibit the form $P(\sigma) \propto |\sigma|^{-3}$ expected of a population of dislocations (Kalácska et al., 2017; Wilkinson et al., 2014). We apply this analysis to the $\sigma_{12}$ component of the stress tensor as this component is the least modified by sectioning the sample and is a shear stress capable of exerting glide forces on dislocations (Wallis et al., 2019). This approach has recently been applied to olivine by Wallis et al. (2021, 2022). We include in these plots data from an undeformed Si wafer measured by Wallis et al. (2022) to provide an indication of the noise level of the stress measurements.

#### 2.5.3. Twin Density Measurements

Twin density was measured using a combination of forescattered electron images and EBSD maps. For each sample for which twin density was reported, we chose between 20 and 60 grains in a representative forescattered electron image, and measured twin spacing and twin width perpendicular to the selected twin set. Using an EBSD map of the same area, we determined the orientation of each grain and active twin set, and used the angle between the normal to the twin plane and the normal to the section to correct the measured twin width and spacing (the same procedure as used by Rutter et al., 2022).

## 3. Results

### 3.1. Mechanical Data and In Situ *P*-Wave Speed

#### 3.1.1. General Characteristics

The stress-strain behavior is qualitatively similar across the range of conditions and tested materials (Figure 2), and is typical of ductile behavior.

**Table 3**
*Continued*

| Experiment | Lithology | $P$ (MPa) | $T$ (°C) | $\sigma_5$ (MPa) | $h_5$ (GPa) |
|---|---|---|---|---|---|
| Run0126 | Wombeyan marble | 574 | 416 | 100 | −0.02 |
| Run0127 | Wombeyan marble | 400 | 392 | – | – |

*Note.* Tests denoted with * are accompanied by measurements of *P*-wave speed parallel to the specimen axis.

Taking the example of Carrara marble at $P$ = 600 MPa and $T$ = 20°C (Figure 2b, solid dark blue curve), the mechanical data are characterized by a rapid linear increase in stress at low strain ($\varepsilon < 0.5\%$), representing elastic loading, during which *P*-wave speed remains relatively constant (Figure 2b, dashed dark blue curve). Above a stress of around 250 MPa, the rate of increase in stress with strain begins to decrease and the *P*-wave speed begins to decrease concomitantly. Beyond approximately 1.5% strain, stress continues to increase approximately linearly with strain, which is accompanied by a steady decrease in wave speed. Similar qualitative behavior occurs in all samples at all conditions tested, with quantitative variations in the yield stress and degree of hardening.

Strain hardening is observed at nearly all test conditions (Figure 2), with the exception of Wombeyan marble deformed at $T$ = 400°C (Figure 2i, solid curves). There is some uncertainty in the strength of Wombeyan Marble at $T$ = 400°C, as the hardening may be obscured by seal friction. Between 20 and 200°C, hardening rates are unaffected by temperature increases, however the hardening modulus is lower for all lithologies at $T$ = 400°C.

### 3.1.2. Effect of Pressure and Temperature

The absolute strength, that is, the differential stress at a given strain, of all rocks tested decreases with increasing temperature. The temperature sensitivity is greater at elevated pressure (400 and 600 MPa) than at low pressure, and is greater in Wombeyan marble than in Carrara marble and Solnhofen limestone (Figure 3).

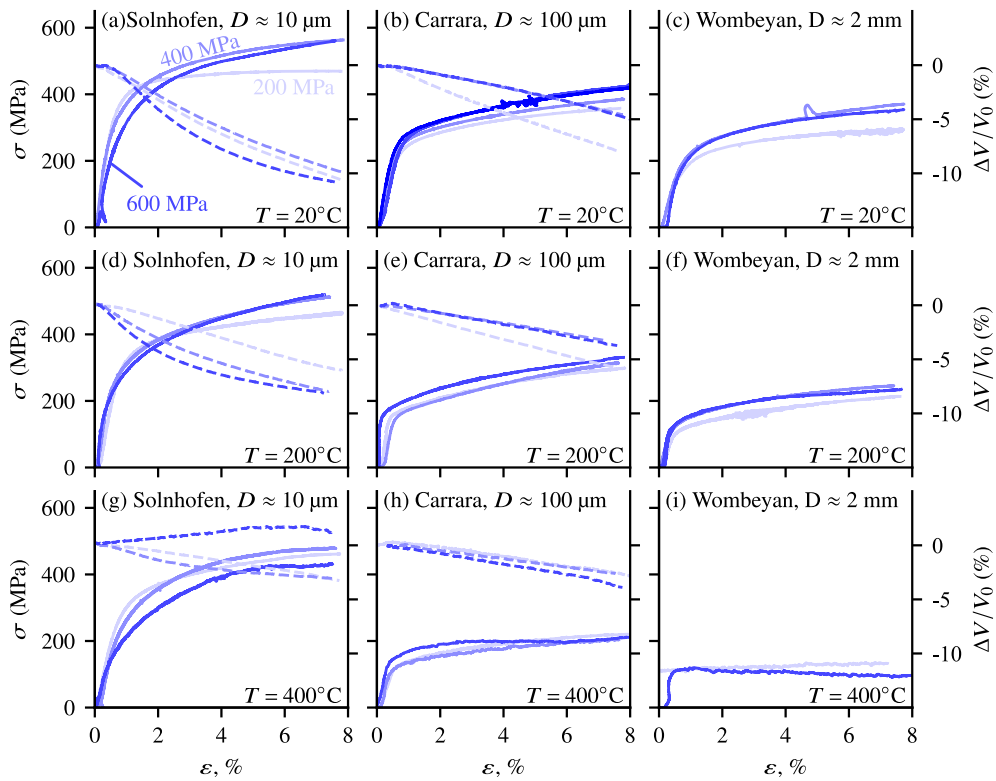


**Figure 2.** Differential stress ($\sigma$, solid lines) and normalized *P*-wave speed ($\Delta V/V_0$, dashed lines) from constant-strain rate experiments at $P$ = 200, 400, 600, and 800 MPa, indicated by increasing intensity of blue, at 20, 200, and 400°C increasing downward in the plot. Plots (a), (d), and (g) correspond to experiments performed on Solnhofen limestone at 20, 200, and 400°C respectively. Plots (b), (e), and (h) are tests performed on Carrara marble at 20, 200, and 400°C respectively. Plots (c), (f), and (i) are tests performed on Wombeyan marble at 20, 200, and 400°C respectively.

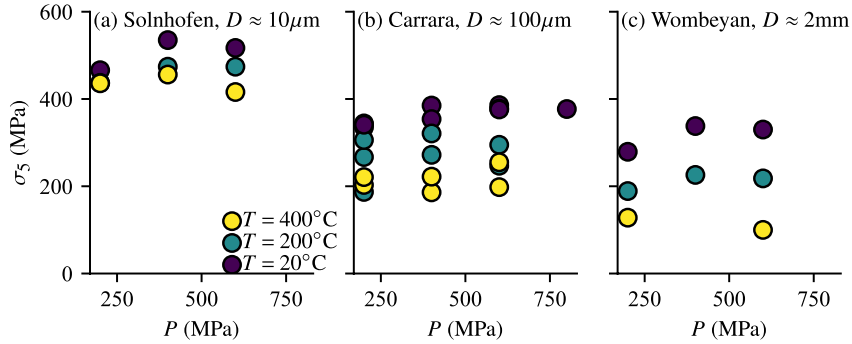


**Figure 3.** Differential stress at 5% strain ($\sigma_5$) as a function of confining pressure in Solnhofen limestone (a), Carrara marble (b) and Wombeyan marble (c), at temperatures of 20, 200, and 400°C. All tests were conducted at a strain rate of $10^{-5}$ s$^{-1}$.

Both Carrara marble and Wombeyan marble have strengths and yield stresses that tend to increase with increasing pressure (Figure 3). However, strength seems to become pressure-independent beyond a pressure threshold. In Carrara marble, there are no quantitative differences between the tests conducted at 600 MPa and at 800 MPa, and only small differences can be detected between 400 and 600 MPa. In Wombeyan marble, strength does not change appreciably with pressure above 400 MPa. The pressure sensitivity of strength in Carrara marble and Wombeyan marble is reduced by increasing temperature, and strength becomes pressure independent at a lower pressure as temperature increases. Hardening rates in Carrara marble and Wombeyan marble also increase with increasing pressure, except for at a temperature of 400°C, at which hardening rates are independent of pressure.

Solnhofen limestone exhibits some differences compared to the other lithologies in terms of the pressure dependence of strength. At all conditions, the yield stress of Solnhofen limestone decreases with increasing pressure, in contrast with the other lithologies. At 5% strain, the strength of Solnhofen limestone increases slightly with pressure from 200 to 400 MPa, but decreases at 600 MPa (Figure 3a).

The evolution in *P*-wave speed also depends on pressure, temperature and rock type. In Carrara marble, wave speeds systematically decrease with increasing strain. The decrease is less marked with increasing pressure and temperature. For example, at a pressure of 200 MPa and strain of 7.5%, the relative wave-speed decrease is 8% at a temperature of 20°C (Figure 2b) and is 2.5% at 400°C (Figure 2h). In Solnhofen limestone, at room temperature and 200°C, the *P*-wave speed decreases with increasing axial strain. With increasing pressure, the decrease tends to be more marked. For example, at 200 MPa and 200°C, the *P*-wave speed drops by about 6% at 7.5% strain, whereas the drop is of about 8% (at the same strain) at 400 and 600 MPa. The *P*-wave speed decreases less with increasing temperature. At 400°C, and 600 MPa, the wave speed even slightly increases with increasing strain (Figures 2a and 2d).

### 3.1.3. Effect of Grain Size

Grain-size has a marked effect on the mechanical behavior. Solnhofen limestone is always the strongest material and Wombeyan marble the weakest, independent of test conditions (Figures 2 and 4). For example, at a temperature of 20°C and pressure of 600 MPa, the stress at 7.5% strain is 570 MPa for Solnhofen limestone, 400 MPa for Carrara marble, and 310 MPa for Wombeyan marble (Figure 4).

The dependence of strength on grain size is further promoted by increases in strain. For example, at a temperature of 20°C the range of stresses across the grain sizes tested is $\sigma_y$ = 100–300 MPa at the yield stress, $\sigma_{2.5}$ = 250–500 MPa at 2.5% strain, and $\sigma_5$ = 300–600 MPa at 5% strain (Figure 4). This observation is consistent with measurements of the hardening modulus, which increases with decreasing grain size at all tested temperatures (Figure 5).

Wave-speed evolution is also sensitive to grain size, as highlighted by comparing the behavior of Solnhofen limestone and Carrara marble. The overall decrease in wave speed is nearly always greater for Solnhofen limestone at a given set of conditions than it is for Carrara marble. For example, at $T$ = 20°C, $P$ = 600 MPa and $\varepsilon$ = 7.5%, the wave-speed change is −5% in Carrara marble (Figure 2b) but is −11% in Solnhofen limestone (Figure 2a). The only exception to this grain-size dependence is at $T$ = 400°C and $P$ = 600 MPa. At these conditions, the final relative wave-speed change at $\varepsilon$ = 7.5% is +2% in Solnhofen limestone (Figure 2g) and −2% in Carrara marble (Figure 2h) dashed dark blue curve.

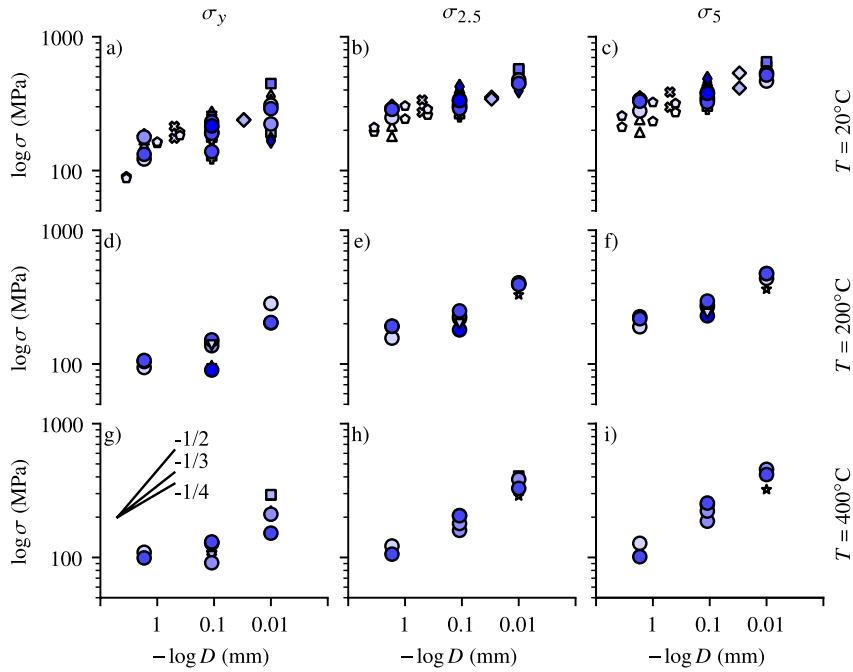


**Figure 4.** Evolution of yield stress ($\sigma_y$), differential stress at 2.5% strain ($\sigma_{2.5}$) and 5% strain ($\sigma_5$) as functions of grain size. Circles correspond to data obtained in this work, and other symbols are taken from the literature (see Table 4 for list of labels).

**Table 4**
*Summary of References for Literature Data Presented in Figures 4 and 5*

| References | Lithology | $D$ (mm) | Legend |
|---|---|---|---|
| Paterson (1958) | Wombeyan marble | 1–2 mm | △ |
| Heard (1960) | Solnhofen limestone | 6–10 μm | □ |
| Edmond and Paterson (1972) | Solnhofen limestone | 6–10 μm | ◇ |
| Edmond and Paterson (1972) | Carrara marble | 60–120 μm | ◇ |
| Fredrich et al. (1989) | Carrara marble | 60–120 μm | ✣ |
| Rybacki et al. (2021) | Carrara marble | 60–120 μm | ▽ |
| Fredrich et al. (1990) | Wombeyan marble | 1–2 mm | ◇ |
| Donath and Fruth (1971) | Beldens marble | 0.5 mm | ✣ |
| Mogi (1964) | Yamaguchi “Fine marble” | 0.4 mm | ⬠ |
| Mogi (1964) | Mito marble | 1 mm | ⬠ |
| Mogi (1964) | Yamaguchi “Coarse marble” | 3.5 mm | ⬠ |
| Rutter (1974) | Solnhofen limestone | 6–10 μm | ☆ |

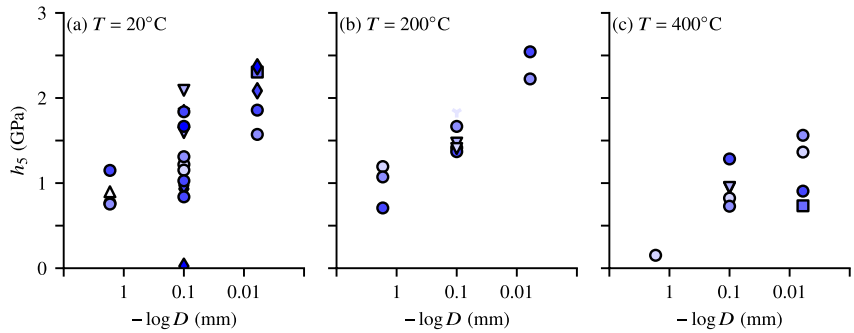


**Figure 5.** Hardening modulus at 5% strain as a function of grain size, at (a) 20°C, (b) 200°C, and (c) 400°C. Circles correspond to data obtained in this work, and other symbols are taken from the literature (see Table 4 for list of symbols).

### 3.2. Wave-Speed Changes During Decompression

Wave speed always decreases significantly during decompression (Figure 6). In Solnhofen limestone, the *P*-wave speed remains approximately constant during initial decompression down to around 400 MPa.

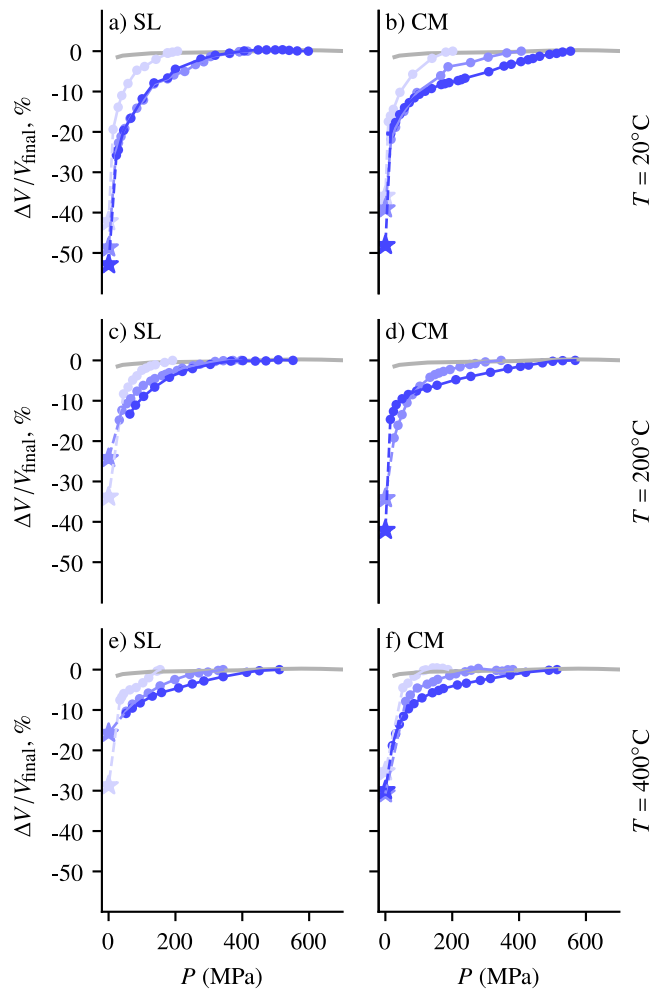


**Figure 6.** Relative change in *P*-wave speed referenced to the final wave speed ($V_{final}$) measured during the unloading phase of each experiment and after sample cooling. Stars denote the wave speed measured at atmospheric pressure after sample recovery. The gray curve represents measurements of wave speed in a fused silica blank over the same pressure range. Curves are colored increasingly blue with increasing pressure. SL is Solnhofen Limestone and CM is Carrara Marble.

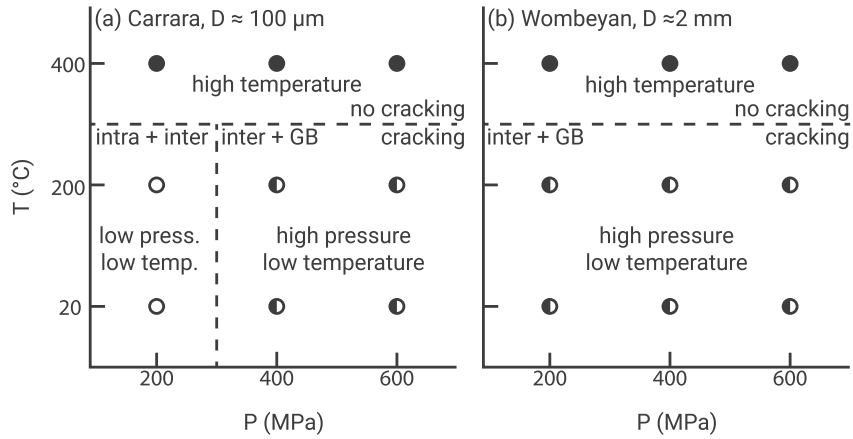


**Figure 7.** Span of microstructural regimes identified in deformed samples.

Further decompression leads to a decrease in wave speed, which drops substantially at pressures below 200 MPa. In samples deformed at room temperature, the wave speed of the recovered material is as low as 50% of the wave speed measured after deformation but prior to decompression. This drop becomes less marked in samples deformed at high temperature, with changes on the order of 25%–35% at $T = 200$°C, and 15%–30% at $T = 400$°C. The behavior is generally similar in Carrara marble, with some notable quantitative differences. The wave speed starts decreasing immediately as pressure in decreased, even in tests conducted at $P = 600$ MPa (Figures 6b and 6d). The characteristic pressure below which $P$-wave speed drops most markedly is on the order of 100 MPa. The effect of deformation temperature is similar to that observed in Solnhofen limestone, with elevated temperature during deformation promoting a more limited reduction in wave speed during decompression.

### 3.3. Microstructures

In this Section, we first summarize the key microstructural features that characterize semi-brittle flow of our samples. Overall, our optical and SEM observations agree well with the large number of previous studies on the subject (e.g., Fredrich et al., 1989; Olsson, 1974; Olsson & Peng, 1976; Rybacki et al., 2021). We then complement the existing work by characterizing the details of intracrystalline deformation using HR-EBSD, which allows us to estimate local dislocation density and internal stress heterogeneity.

#### 3.3.1. Brittle Features

Systematic observations of cracks within deformed samples reveals three distinct deformation regimes according to deformation conditions (Figure 7). The low-pressure, low-temperature regime and the high-pressure, low-temperature regime are characterized by cracks, whereas in the high-temperature regime cracks are absent.

In the low temperature regimes where cracks are observed, cracks interact with twins. Dense arrays of cracks confined to individual twin lamellae are commonly observed (Figure 8c). In addition, some intragranular cracks contain steps and change orientation across individual twin lamellae ("stair-step," Figure 8e). In other instances, microcracks are observed to nucleate from the tips of twins, and do not reach grain boundaries (Figure 8f).

##### *3.3.1.1. Low-Pressure, Low-Temperature Regime*

The low-pressure, low-temperature regime is limited to Carrara marble experiments conducted at 200 MPa and 20 and 200°C only. In this regime mode-I intragranular microcracks are a common feature, and result in the highest crack densities. These microcracks are typically confined to single grains and are of low aspect ratio (e.g., Figures 8b and 8d). In places, the microcracks are concentrated in discrete regions as crush zones (Figure 8a). In these regions, cracks often span a few grains and result in a locally elevated crack density.

Cracks are also observed to relate to the geometry of grains and grain boundaries. Some cracks nucleate at geometric irregularities along grain boundaries. For example, steps in grain boundaries are often associated with short tensile cracks that propagate a short distance into the grain interior (Figure 8d). Smaller grains can also act

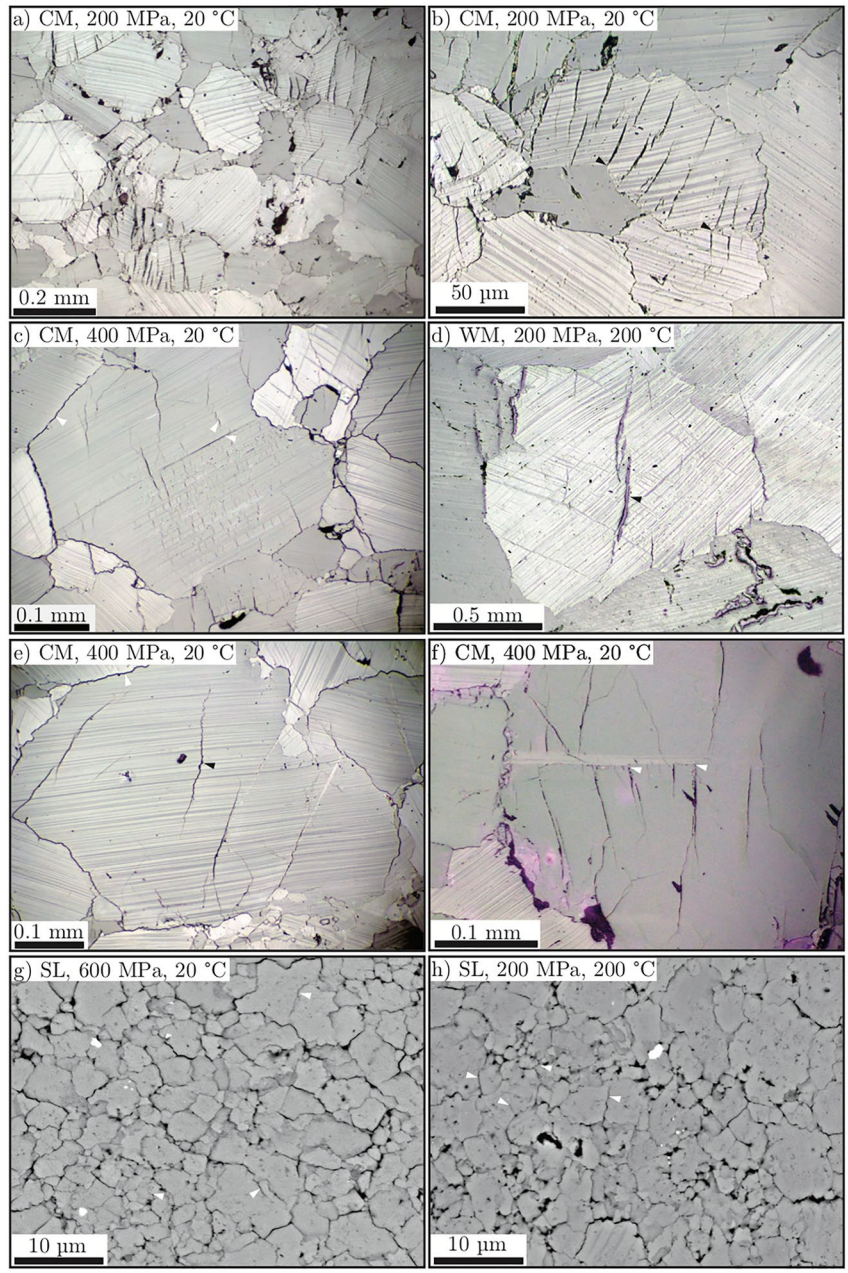


**Figure 8.** Brittle microstructures observed in samples after testing, using visible light (a–f) and scanning electron (backscattered electrons, g and h) microscopy. (a) Crush zones, (b) geometrically controlled cracks, (c) inter-twin cracks and stair-step cracks, (d) grain-boundary cracks and low aspect-ratio cracks, (e) stair-step cracks with orientations controlled by twin boundaries, and (f) cracks nucleated from twins.

as indenter grains, and cracks are nucleated to accommodate the indenter grain shape (Figure 8b). Often, cracks relating to geometric incompatibilities can be wholly contained within a single grain (Figures 8b and 8d).

#### *3.3.1.2. High-Pressure, Low-Temperature Regime*

The high-pressure, low-temperature regime spans samples deformed above $P = 200$ MPa and at $T = 20°$ and 200°C for Carrara marble, and all samples deformed at 20 and 200°C for Wombeyan marble (Figure 7). This regime is characterized by a reduced crack density ($S_v < 8$ mm$^2$/mm$^3$) with respect to the low-pressure, low-temperature regime. Intragranular cracks are not completely suppressed (Figures 8d–8f). However, thorough observations revealed no intergranular cracking and crush zones. Another important change compared to the low-pressure,

**Table 5**
*Crack Densities, $S_v$, in Selected Samples as the Volumetric Number of Cracks Determined From Stereological Measurements Following Underwood (1970)*

| Sample | Lithology | $P$ (MPa) | $T$ (°C) | $S_v$ (mm$^2$/mm$^3$) |
|---|---|---|---|---|
| Run0075 | CM | 200 | 19.8 | 18.73 |
| Run0078 | CM | 405 | 19.8 | 7.31 |
| Run0084 | CM | 615 | 19.8 | 2.28 |
| Run0086 | CM | 236 | 197 | 7.60 |
| Run0090 | CM | 213 | 390 | 2.05 |
| Run0093 | CM | 599 | 192 | 7.82 |
| Run0094 | CM | 594 | 401 | 1.30 |
| Run0098 | CM | 769 | 20.1 | 4.60 |
| Run0104 | WM | 206 | 19.3 | 4.02 |
| Run0106 | WM | 595 | 20.2 | 0.33 |
| Run0110 | WM | 231 | 207 | 1.51 |
| Run0119 | WM | 609 | 187 | 0.49 |
| Run0120 | WM | 408 | 19.2 | 1.60 |
| Run0121 | WM | 428 | 190 | 0.35 |
| Run0124 | WM | 233 | 408 | 0.47 |
| Run0126 | WM | 574 | 416 | 0.36 |

*Note.* CM is Carrara marble and WM is Wombeyan marble.

low-temperature regime is the abundant observation of open grain boundaries (Figures 8c and 8e).

Within the high-pressure, low-temperature regime, the crack density decreases with increasing pressure for Carrara marble and Wombeyan marble. For example, in Carrara marble at 20°C, $S_v$ = 7.31 mm$^2$/mm$^3$ at $P$ = 400 MPa reducing to $S_v$ = 2.28 mm$^2$/mm$^3$ at $P$ = 600 MPa (Table 5, Run0078 and Run0084). Furthermore, for a given set of conditions in the high-pressure, low-temperature regime, crack density is lower in the coarser grained Wombeyan marble.

### 3.3.2. Crystal-Plastic Microstructures

Crystal-plastic microstructural features are dominated by deformation twins that are present in samples deformed at all conditions (Figure 9). Nearly all grains are twinned on at least one plane, grains that contain two twin sets are also common, and occasionally grains contain three twin sets. In particular, the density of twins, that is, the number of lamellae per unit length, is high in samples deformed at low temperature (Figure 9a–9d) and decreases with increasing temperature (Figures 9g and 9h). Twins are often curved, especially in the vicinity of grain boundaries (Figure 9f) or around geometric irregularities (Figure 9b). Twins also often appear to have nucleated from twins within neighboring grains (Figures 9b and 9d) or from geometric irregularities at grain boundaries (Figure 9f).

On a larger scale than twin lamellae, undulose extinction is widespread (Figure 9). In Wombeyan marble, the intensity of the undulose extinction increases when approaching grain boundaries and grain-boundary irregularities (Figure 9c). In Wombeyan marble, the undulose extinction observed in some instances suggests corrugation of the crystal lattice (Figure 9e). In Carrara marble, grains also display undulose extinction, although it is not as common as in Wombeyan marble. Again, in Carrara marble undulose extinction is associated to geometric irregularities (Figure 9h).

### 3.3.3. SEM Observations

Forescattered electron images were used to image twins at high spatial resolution. These images reveal very thin deformation twins, especially in Solnhofen limestone, which in some places are on the order of 100 nm in thickness (Figures 10a and 10b). Grains of calcite in Solnhofen limestone also exhibit lower twin incidence than the coarser-grained samples of Wombeyan marble and Carrara marble (Figures 10c and 10d). Twins in Solnhofen limestone also propagate across grain boundaries, and are not bent on the grain scale, although they do sometimes taper in proximity to grain boundaries. High-resolution electron images of Wombeyan marble reveal multiple scales of twins, with micrometer-scale twins contained within thicker twins on the order of tens of micrometers in thickness (Figure 10c).

Overview EBSD maps demonstrate that most grains have significant internal misorientation. Lattice curvature is particularly obvious in Wombeyan marble (Figure 11a) and in Carrara marble (Figure 11b) and in some grains of Solnhofen limestone (Figure 11c). Regions of lattice curvature are often related to the geometry of grain boundaries and in places curvature increases in the vicinity of grain boundaries. Other grains exhibit lattice rotation in the vicinity of twin planes, indicated by stripes in the inverse pole figure map (e.g., Figure 11b).

Further evidence of internal lattice distortion is revealed by maps of the grain reference orientation deviation (GROD), which is the misorientation of each point with respect to the mean orientation of the grain (Figure 12). An overview map of the GROD in Carrara marble Run0093, deformed at a pressure of 600 MPa and temperature of 200°C demonstrates that individual grains have variable internal structure (Figure 12a). Some grains exhibit striped patterns of variable GROD that follow the local twin orientation (Figure 12c). In other grains, the GROD pattern is largely unaffected by twins and instead exhibits lattice distortion over larger length scales approaching the grain size (Figure 12d). In some cases, there is a mixed interaction, where the GROD weakly follows the twin orientation but is also affected by the grain geometry (Figure 12b).

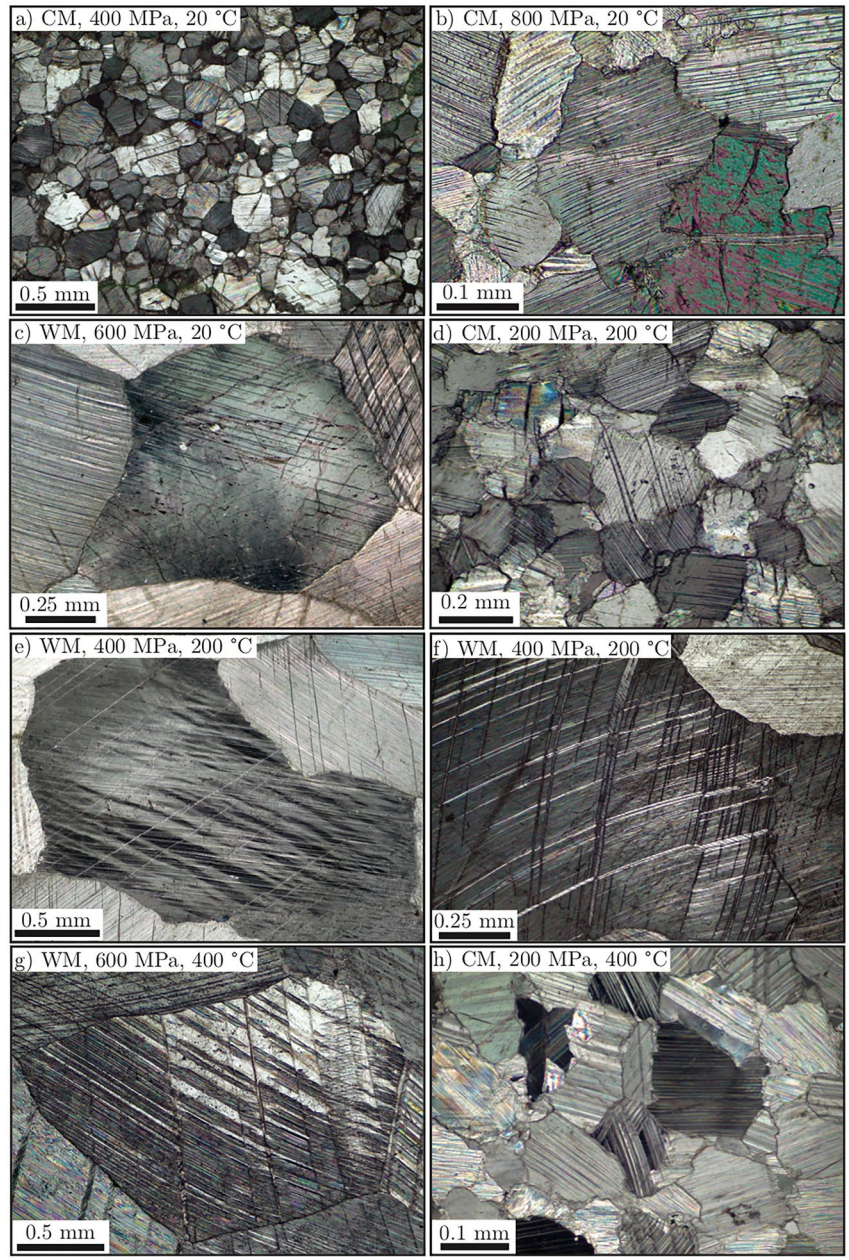


**Figure 9.** Visible light micrographs of (a) High twin density generated at high-stress, low-temperature conditions. (b) High-density twins bending around an apparent deformation band. Twins are also nucleated by twins in neighboring grains. (c) Long-range undulose extinction traversing twin sets. The undulose extinction appears to be generated by the interaction of neighboring grains. (d) Multiply-twinned grains and high twin density. (e) Corrugation of crystal lattice identified by wavy undulation. (f) Multiple curved twin sets and twinned twin sets. (g) Multiply-twinned grain in Wombeyan marble. Twins are thicker than at lower-temperature conditions and also appear more patchy. (h) Twins formed at high temperature in Carrara marble. Twins are thicker and the central grain shows evidence of undulose extinction.

HR-EBSD maps (Figure 13) reveal the distributions of GNDs and intragranular stress heterogeneity in the endmember grains in Figure 12. The grain in Figure 12b, which exhibited the least impact of the twins on the distribution of GROD, also exhibits negligible impact of the twins on GND density (Figure 13a). Within the grain interior, GND density is generally at or below the background noise level of approximately $10^{13.5}$ $m^{-2}$ arising from noise in the rotation measurements. Apparent GND densities above this noise level are highly localized in the vicinity of twin boundaries and potentially result from reduced pattern quality indicated by the band-contrast

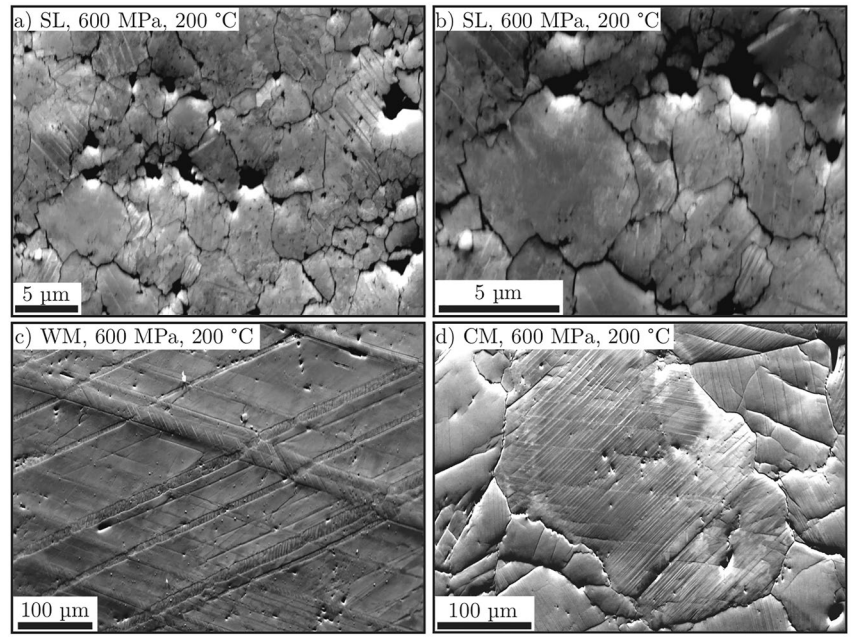


**Figure 10.** Forescattered-electron orientation-contrast images (Prior et al., 1996) of deformation twins in (a, b) Solnhofen limestone, (c) Wombeyan marble and (d) Carrara marble.

map. However, GND densities are significantly elevated to the order of $10^{14}$ $m^{-2}$ adjacent to a grain boundary along the right edge of the map. Comparable distributions are evident in the maps of stress heterogeneity with stresses in the grain interior being relatively homogeneous and stresses near the grain boundary being elevated to several hundred megapascals. Different distributions are apparent in HR-EBSD maps (Figure 13b) from within the grain in Figure 12c, which exhibited the greatest impact of the twins on the distribution of GROD. In this grain, zones of elevated GND density and stress extend a few micrometers from the twin boundaries and beyond the zones of reduced pattern quality represented in the band-contrast map. Within these zones, GND densities approach $10^{14}$ $m^{-2}$ and shear stresses on the order of several hundred megapascals are common.

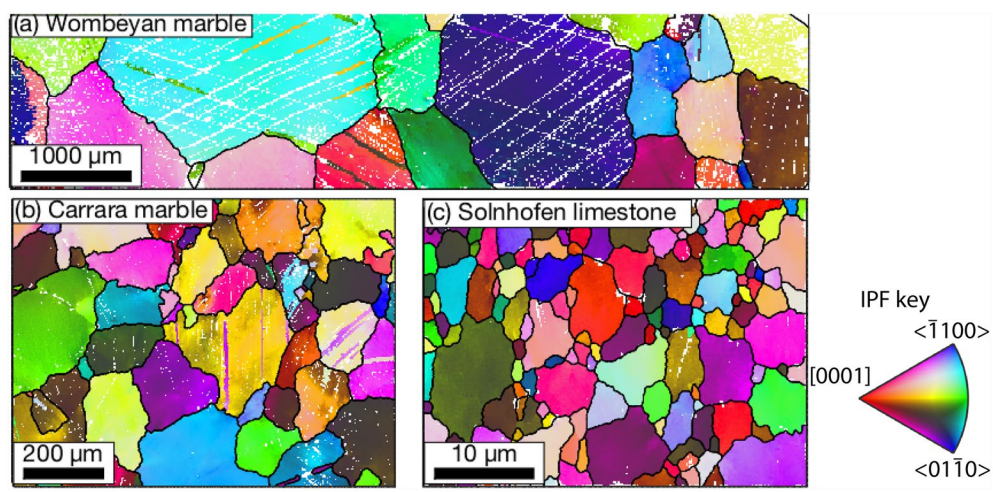


**Figure 11.** Electron backscatter diffraction maps of samples deformed at a pressure of 600 MPa and temperature of 200°C. (a) Wombeyan marble, (b) Carrara marble, and (c) Solnhofen limestone. Grains are colored according to the inverse pole figure. Twin boundaries are not shown for clarity. White areas were not indexed and are mostly due to poor quality diffraction patterns along twin boundaries.

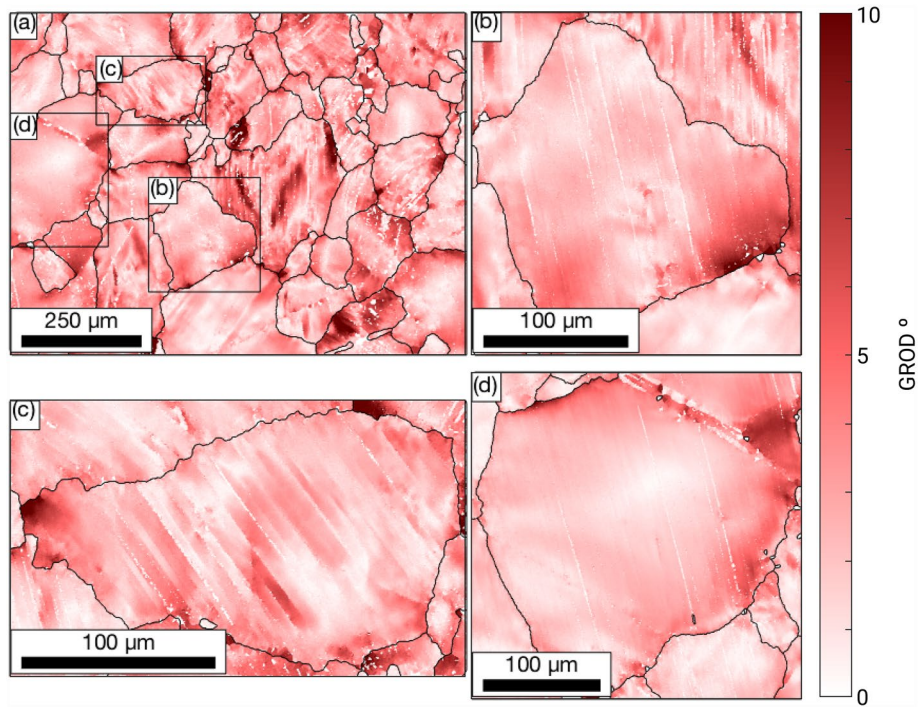


**Figure 12.** Map of grain reference orientation deviation (GROD) obtained from electron backscatter diffraction (EBSD) maps of Run0093 ($P = 600$ MPa, $T = 200$°C). Insets (b–d) are small-area EBSD maps showing the local GROD within grains with varying interaction between lattice distortion and twins. Strong interactions between twins and lattice curvature are evident in (c), intermediate interaction is present in (b), and weak interaction is apparent in (d). Insets (b) and (d) also exhibit significant lattice curvature in the vicinity of grain boundaries.

The probability distributions of the stress heterogeneity provide further information on the cause of the stresses. The normal probability plot (Figure 13c) exhibits similar probability distributions for both grains, with stresses that are significantly greater than those measured on the undeformed Si standard. Below stress magnitudes of approximately 300–500 MPa, the distributions fall on a straight line indicating these stresses are normally distributed. However, at greater stress magnitudes, the distributions depart from straight lines. These high-stress tails are typical of materials, including Cu and olivine, deformed by dislocation-mediated mechanisms (Jiang et al., 2013; Wallis et al., 2021, 2022). The plot of the restricted second moment $\nu_2$ versus $\ln(\sigma_{12})$ provides a further test of whether these high-magnitude stresses are the stress fields of dislocations (Figure 13d). On this plot, the distributions from the maps from each grain both fall on straight lines at high stresses, indicating that the distributions have the $P(\sigma) \propto |\sigma|^{-3}$ form that is characteristic of the stress field of a population of dislocations (Groma & Bakó, 1998; Kalácska et al., 2017; Wallis et al., 2021; Wilkinson et al., 2014). These characteristics indicate that the stresses are, at least in part, the stress fields of dislocations.

In addition to the EBSD mapping, based on the forescatter imaging, we were able to measure twin spacing and correct their thickness in the same manner as Rutter et al. (2022, Figure 14). We report values of twin density, $\rho_t$ (mm$^{-1}$), which is computed as the inverse of the measured average twin spacing (Figure 14b). Our data agree with previously reported measurements of stress versus twin density. Twin density is lowest in Wombeyan marble deformed at a pressure of 600 MPa and temperature of 200°C with a value of 130 mm$^{-1}$, equivalent to a mean spacing of 7.5 µm. The highest density is obtained for Solnhofen limestone deformed at 600 MPa and 200°C, with a value of about 1,500 mm$^{-1}$, equivalent to a mean twin spacing of 0.7 µm.

## 4. Discussion

The mechanical data reveal that deformation of calcite rocks across the range of conditions that we tested is ductile. Almost all experiments demonstrate strain-hardening behavior but the precise characteristics of the hardening vary with pressure and temperature. The deformation of calcite rocks in this study is accommodated by

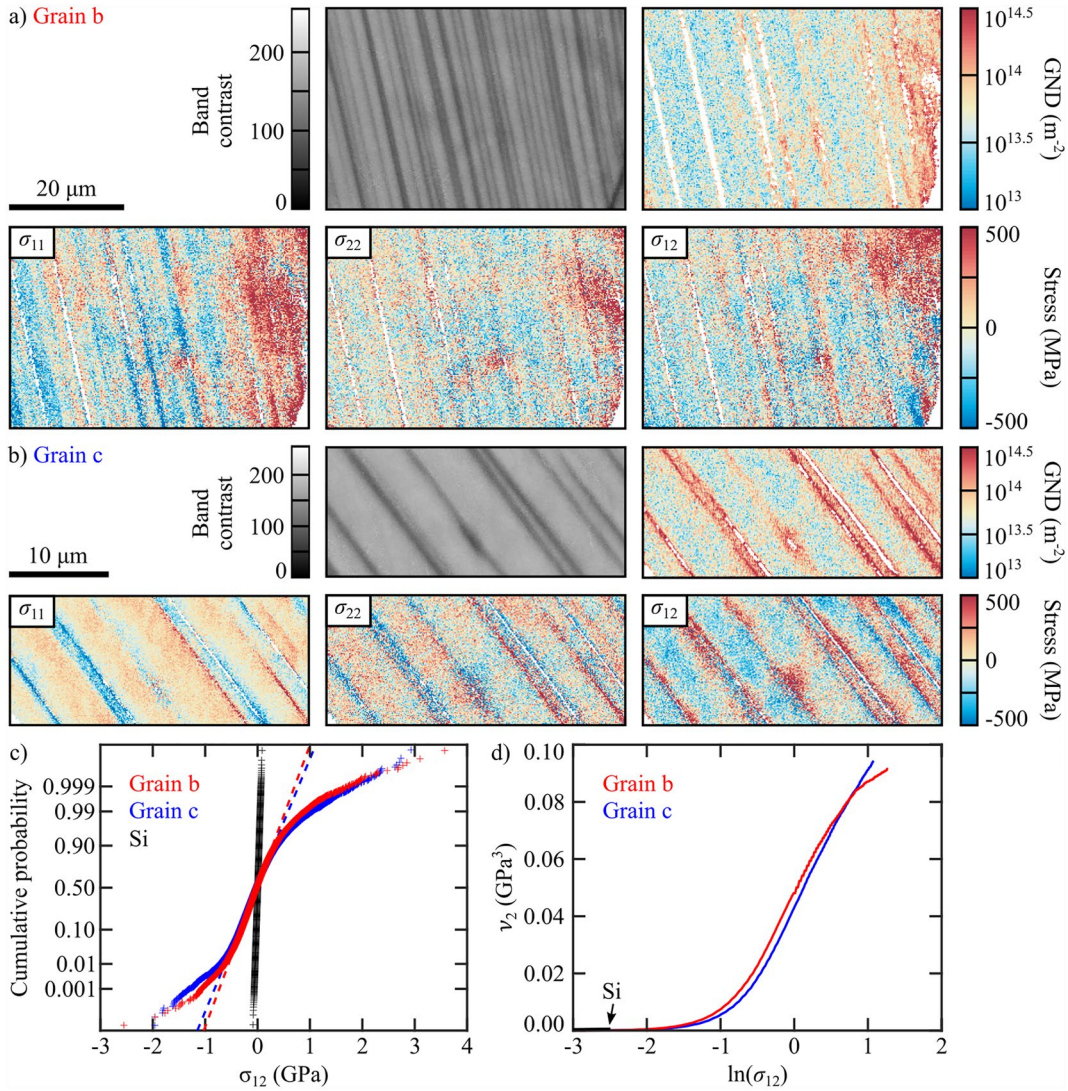


**Figure 13.** HR-EBSD maps of (a) the grain in Figure 12b and (b) the grain in Figure 12c. Each of these subfigures presents maps of the band contrast in the diffraction patterns, which reveals the locations of twins, geometrically necessary dislocation density, and heterogeneity in stress ($\sigma_{ij}$). (c) Normal probability plot of $\sigma_{12}$ in each grain. Straight lines indicate a normal distribution. (d) Restricted second moment ($\nu_2$) versus ln$\sigma_{12}$. Straight lines indicate that the probability distribution of the stress exhibits the form $P(\sigma) \propto |\sigma|^{-3}$ expected of a population of dislocations.

cracking, twinning and dislocation motion, depending on experimental conditions. The main question we seek to answer is what controls the rheological behavior of calcite rocks in the semi-brittle regime? Determination of the rheological behavior of calcite rocks requires knowledge of the approximate partitioning of strain between each active deformation mechanism. This can be answered by considering the microstructural, wave-speed, and mechanical data.

### 4.1. Brittle Deformation

The evolution of wave speed combined with post-mortem measurements of crack density characterize the degree of microcracking occurring during deformation. At all temperatures at which strength is pressure sensitive, increasing pressure results in increasing hardening rates, smaller wave-speed decreases and a reduction in *post-mortem* crack density (Figure 15 and Table 5). Similar observations of decreasing *post-mortem* crack density with increasing pressure were made by Fredrich et al. (1989) in Carrara marble at room temperature. Measurements of volumetric strain during the deformation of Carrara marble and Solnhofen limestone at room

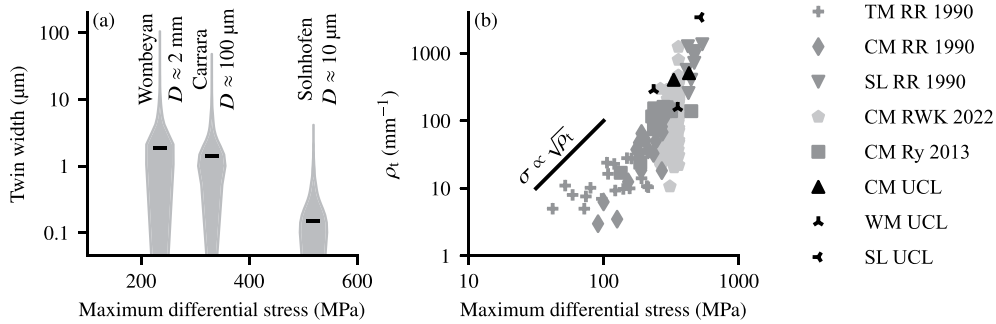


**Figure 14.** The final differential stress at the end of deformation as a function of twin density for this study is shown in black symbols. Additional data from previous studies are shown in gray. CM RR 1990, TM RR 1990, and SL RR 1990 are data from Carrara marble, Taiwan marble, and Solnhofen limestone by Rowe and Rutter (1990), CM RWK 2022 is data from Carrara marble data by Rutter et al. (2022), and CM Ry 2013 is data from Carrara marble by Rybacki et al. (2013). The reference line indicates the gradient of a relationship in which stress is dependent on the square root of twin density.

temperature made by Edmond and Paterson (1972) demonstrate that dilatancy is suppressed at high pressure. Both these studies also report increased hardening rates with increasing pressure. Decreasing strain accommodation by cracking is therefore systematically associated with increasing hardening rates (Figure 15).

The behavior of Solnhofen limestone is impacted by the existence of a nonnegligible equant porosity of about 4%. The existence of this small porosity is expected to impact the volumetric strain behavior, with an initial yielding in compaction as documented by Baud et al. (2000). Our data set exhibits some manifestations of compaction yielding. There is an inverse pressure dependency of the wave-speed evolution, with the wave speed dropping more at high pressure, potentially due to enhanced microcracking during pore collapse. In addition, the wave speed increases during deformation at 400°C and 600 MPa, which can be attributed to deformation-induced compaction and crack closure. Despite these small quantitative differences, the overall behavior of Solnhofen limestone remains broadly similar to that of Carrara marble, with a macroscopically ductile behavior, strain hardening and a trend toward decreasing *P*-wave speeds with increasing strain (except at the highest tested temperature and pressure).

With increasing temperature, pressure-independent strength is reached at a lower pressure. In conjunction with this, deformation at elevated pressure is systematically related to smaller drops in wave speed and increased hardening rates. Crack density is also lower for a given pressure at higher temperature. Measurements of reduced pore volume during deformation of Carrara marble at high temperatures by Fischer and Paterson (1989) support this observation. Taken together, these observations show that cracking is suppressed by temperature increases.

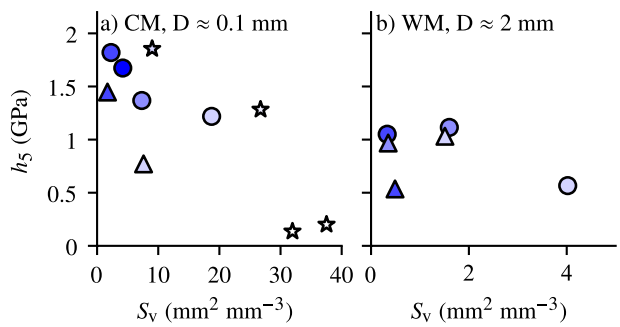


**Figure 15.** Hardening modulus computed at 5% strain plotted against post-mortem crack densities. (a) Carrara marble data from room-temperature experiments (circles this study, stars Fredrich et al. (1989)) and at 200°C (triangles). (b) Wombeyan marble from experiments at room temperature (circles) and 200°C (triangles).

Another interesting observation is the large wave-speed decrease during decompression, after cooling of the samples. This feature suggests that significant sample damage is accrued during decompression. Our measurements are performed only in the axial direction, and are thus not sensitive to axial microcracks, which develop preferentially during axial shortening in the semi-brittle regime (Fredrich et al., 1989; Meyer et al., 2021; Schubnel et al., 2005). Despite this limitation, the changes observed are remarkably large (several tens of percent), which indicates intense microcracking. Samples with the largest wave-speed decrease are those deformed at high-pressure, low-temperature conditions, which correspond to a low intragranular fracture density (Table 5). These samples are characterized by open grain boundaries (Figures 8b, 8c, 8e, and 8g), suggesting that grain-boundary opening is the cause of the observed wave-speed decrease. Similar observations were made by Edmond and Paterson (1972), who reported increases in volumetric strain during decompression in deformed Solnhofen limestone and Carrara marble, with the magnitude of volumetric strain change increasing with the final stress level. This phenomenon is likely to result from deformation caused by strain incompatibility between grains (Ashby, 1970). During deformation at

high pressure, individual grains deform both plastically and elastically to accommodate the imposed strain in the sample, which results in heterogeneous internal stresses. Upon removal of the confining pressure, these internal stresses are no longer in equilibrium with the applied external forces and are likely to generate interface cracks between grains to accommodate the strain incompatibilities accrued during deformation.

### 4.2. Grain-Size Sensitive Behavior

Our results demonstrate that yield stress and the hardening modulus are functions of grain size. This result is consistent with the works of Olsson (1974) and Fredrich et al. (1990) and other published results at both low temperatures (Donath & Fruth, 1971; Edmond & Paterson, 1972; Fredrich et al., 1989; Heard, 1960; Mogi, 1964; Paterson, 1958; Rutter, 1974; Rybacki et al., 2021; Figure 4 and Table 4) and high temperatures (Renner et al., 2002).

Based on experiments at room temperature and moderate pressure, Fredrich et al. (1990) discussed the strength increase with decreasing grain size in the model framework of Horii and Nemat-Nasser (1986). Horii and Nemat-Nasser (1986) solved a wing-crack model coupled to a "plastic zone," and their results predicted that coarser-grained materials should be more "brittle," that is, the ratio of differential stress to confining pressure at the brittle-ductile transition should decrease with increasing grain size. The results of Fredrich et al. (1990) showed that this ratio was independent of grain size, which they explained by considering that the plastic yield stress scaled as $D^{-1/2}$. This hypothesis is supported by our observations. More generally, yield stress is observed to scale inversely with grain size in metals (Cordero et al., 2016) and also in olivine (Hansen et al., 2019).

Strengthening with decreasing grain size is a common phenomenon in metals and has received significant attention in the metallurgy literature (see Cordero et al. (2016) and Y. Li et al. (2016) for reviews). Strengthening with decreasing grain size is usually termed the Hall-Petch effect (Hall, 1951; Petch, 1953), and is typically of the form

$$\sigma = \sigma_0 + K D^m, \tag{1}$$

where $\sigma_0$ is the intrinsic resistance of a lattice to dislocation motion, $K$ is a material-dependent Hall-Petch coefficient and $m$ is a dimensionless exponent. In the original observations and theoretical arguments of Hall (1951) and Petch (1953), the exponent $m = -0.5$. Values of $m = -1$ to $-0.2$ have been reported in metals (Cordero et al., 2016; Dunstan & Bushby, 2014; Y. Li et al., 2016).

We fitted Equation 1 to our data using a least-squares regression and setting $m = -0.5$ (Table 6), similar to Renner et al. (2002). Although our results suggest $m$ in the range $-0.6$ to $-0.3$ (Figure 4), fitting the exponent significantly modifies $\sigma_0$ and $K$ and makes comparison among our datasets challenging. Values of the apparent lattice resistance, $\sigma_0$, and the Hall-Petch coefficient, $K$, increase with strain at all temperatures. Values of the lattice resistance are largest at $T = 20$°C, with $\sigma_0 = 155$–$274$ MPa, and are smaller at $T = 200$°C with $\sigma_0 = 83$–$185$ MPa, further reducing at 400°C to $\sigma_0 = 68$–$108$ MPa. The values for the lattice resistance are consistent with measurements from single-crystal experiments by J. H. De Bresser (1991) and Turner et al. (1954) at the same temperatures. Values of the Hall-Petch coefficient are largely unaffected by temperature changes. For the reported values of $\sigma_y$, $K = 0.4$–$0.52$ MPa m$^{-0.5}$, at larger strain for values of $\sigma_{2.5}$ the Hall-Petch coefficient increases to $K = 0.72$–$0.86$ MPa m$^{-0.5}$ with further increases at large strain of $K = 0.79$–$0.96$ MPa m$^{-0.5}$ for $\sigma_5$ values. When $K$ is normalized by the product of the shear modulus $G$ and Burgers vector $b$, with $G = 35$ GPa and $b = 0.74$ nm, it falls into the range 0.42–1, which is consistent with values typically obtained for body centered cubic and hexagonally close packed metals (Cordero et al., 2016). In summary, our data combined with literature sources reveal several key features of the Hall-Petch effect in calcite rocks, (a) the Hall-Petch effect is amplified by strain, being weakest at yield and strong after plastic strain, (b) the apparent lattice resistance increases with plastic strain and decreases with temperature, and (c) the Hall-Petch coefficient is independent of temperature (in the range investigated).

**Table 6**
*Results of Fitting Collated Mechanical Data With the Hall-Petch Relation, With $m = -0.5$ (Equation 1)*

| Variable | $\sigma_0$ (MPa) | $K$ (MPa m$^{-0.5}$) |
|---|---|---|
| $T = 20$°C | | |
| $\sigma_y$ | 155 | 0.40 |
| $\sigma_{2.5}$ | 244 | 0.73 |
| $\sigma_5$ | 274 | 0.87 |
| $T = 200$°C | | |
| $\sigma_y$ | 83 | 0.51 |
| $\sigma_{2.5}$ | 149 | 0.72 |
| $\sigma_5$ | 185 | 0.79 |
| $T = 400$°C | | |
| $\sigma_y$ | 68 | 0.52 |
| $\sigma_{2.5}$ | 91 | 0.86 |
| $\sigma_5$ | 108 | 0.96 |

Extensive reviews by Cordero et al. (2016) and Y. Li et al. (2016) summarize proposed physical models of the Hall-Petch effect. Y. Li et al. (2016) identify four categories of models: (a) the dislocation pile-up model, in which grain boundaries act as obstacles that cause pile-ups until the stress in front of the pile-up is sufficient to induce yielding of neighboring grains (Hall, 1951; Petch, 1953); (b) the grain-boundary ledge model, in which grain- and subgrain-boundary irregularities emit forest dislocations that act as obstacles (see J. C. Li, 1963); (c) the plastic-strain model, in which the rate of increase in dislocation density with plastic strain is inversely proportional to grain size (Conrad et al., 1967); (d) the elastic-anisotropy model, in which interactions among elastically anisotropic grains require the introduction of GNDs, and smaller grains have relatively larger strain gradients and greater GND densities (Meyers & Ashworth, 1982). All of these models, except that of Meyers and Ashworth (1982), arrive at an expression similar to Equation 1. The coefficient $K$ always includes the shear modulus, $G$, and the Burgers vector, $b$, as well as other geometric constants, and $m = -0.5$. However, fitting exercises have shown that for a wide range of metals, $m \neq -0.5$ and may be better fit by $m = -1$ or by the relationship $\ln d/d$ (Dunstan & Bushby, 2014; Y. Li et al., 2016).

It is not clear which model is the most appropriate for calcite. In general, all the models rely on grain boundaries as sites of dislocation accumulation, either by causing pile-ups or by acting as sources for more dislocations. It is likely that these processes act in concert. In the absence of recovery processes, finite plastic strain inevitably requires the accumulation of GNDs, the density of which depends on grain size (Ashby, 1970). Our microstructural observations and wave-speed data are compatible with this concept. Open grain boundaries (Figures 8c, 8e, and 8g) and large wave-speed decreases during decompression (Figure 6) suggest significant relaxation of internal stress during decompression and, in turn, this internal stress may result from elastic mismatch among grains and associated GND formation. Under the visible-light microscope, we observe undulose extinction that is often correlated to the geometry of grain boundaries (Figure 9), indicating that lattice misorientation (reflecting dislocation activity) is influenced by grain boundaries, although it does not identify whether grain boundaries act as dislocations sources. EBSD observations also reveal significant lattice curvature (Figure 12) and increases in GND density in the vicinity of grain boundaries (Figure 13). Furthermore, microscale observations of strain in deformed calcite rocks by Spiers (1979) and Quintanilla-Terminel and Evans (2016) reveal local heterogeneity in finite strain near to grain boundaries. In particular, Quintanilla-Terminel and Evans (2016) identify strain heterogeneity on a scale similar to the grain size. Wallis et al. (2018) observed an increase in misorientation in the vicinity of grain boundaries in naturally deformed calcite rocks, consistent with the presence of plastic strain gradients imparted in response to strain incompatibility among neighboring grains (Meyers & Ashworth, 1982).

In general, the Hall-Petch effect is traced to the impact of grain boundaries on the dislocation mean free path, either directly (i.e., grain boundaries causing pile-ups) or indirectly (grain boundaries being sources of more dislocations that eventually impede dislocation motion). The observations summarized above are in support of this idea, but do not include the role of twins. To go further in our interpretation, it is useful to turn to a more general class of models (Kocks, 1966, 1976; Mecking & Kocks, 1981) that incorporate directly the role of dislocation mean free path and its dependency on grain size, twin spacing, and dislocation density. In the following, we use the Kocks-Mecking-Estrin (KME) single state-variable approach to explore the relative roles of grain size and twins on strength in calcite.

### 4.3. Is TWIP Compatible With the Deformation of Calcite Rocks?

The activity of mechanical twinning in calcite is closely related to the magnitude of differential stress (Jamison & Spang, 1976; Rowe & Rutter, 1990; Spiers, 1979). In experiments, Rowe and Rutter (1990) demonstrated that the spacing of twins decreases with increasing stress, independent of temperature and grain size. Twins are observed in all our deformed samples, and twin density increases with differential stress consistently with the observations of Rowe and Rutter (1990), Rybacki et al. (2013), and Rutter et al. (2022). Rybacki et al. (2013) also demonstrated that stress was proportional to the square root of twin density at low stresses (<250 MPa). However, at high stress, the value of stress saturates with respect to twin density and the square root dependence breaks down (Rowe & Rutter, 1990, and Figure 14). Transmission Electron Microscope observations of calcite deformation twins indicate that twins often interact with dislocations (Barber & Wenk, 1979; Fredrich et al., 1989; Rybacki et al., 2013). Given these observations, Rybacki et al. (2021) argued that twin spacing linearly decreases as dislocation density increases, as flow stress is proportional to the square root of dislocation

density (Taylor, 1934). These observations suggest that twin spacing either is a consequence of, or controls, the strength of calcite rocks.

Rybacki et al. (2021) argued that twin spacing exerts a control on the strain hardening rate, and by extension the strength, by drawing analogy to twinning induced plasticity steels (TWIP, De Cooman et al., 2018). Models of TWIP originate from high manganese steels, which exhibit high hardening rates (approx. 3% of the shear modulus) with respect to other steels (approx. 0.05% of the shear modulus), as a consequence of mechanical twinning. The mechanism of TWIP originates from the abrupt changes in crystallographic orientation at twin boundaries, which can act as barriers to dislocation motion. Progressive twinning leads to dynamic refinement of the microstructure (De Cooman et al., 2018), in which finer twin spacing reduces the mean free path of dislocations ($\lambda$) and causes a dynamic Hall-Petch effect.

In phenomenological models of TWIP in the metallurgical literature, strain hardening is attributed to a dynamic Hall-Petch effect resulting from progressive twinning (Bouaziz et al., 2008). The model of Bouaziz et al. (2008) is formulated by first considering the Taylor equation that relates shear flow stress ($\tau$) to the total dislocation density ($\rho$),

$$\tau = \tau_0 + \tau_b + \alpha \mu b \sqrt{\rho}, \tag{2}$$

where $\tau_0$ is the initial strength of a polycrystal, $\tau_b$ is the back stress, which may arise from long-range dislocation interactions and stress fields around twins, $\alpha$ a constant close to unity, $b$ the Burgers vector and $\mu$ the shear modulus. In their formulation, the final term represents isotropic hardening due to short-range dislocation interactions. In calcite, the Taylor equation has been demonstrated to apply to calcite rocks deformed at temperatures of 550–700°C (J. H. P. De Bresser, 1996), although the relative contributions of kinematic hardening due to long-range dislocation interactions that generate back stress and isotropic hardening due to short-range dislocation interactions have not been separated.

To obtain the evolution of stress with strain, the Taylor relation is combined with a modified Kocks-Mecking-Estrin equation (Kocks, 1966, 1976; Mecking & Kocks, 1981) to describe the change of $\rho$ with strain (Bouaziz et al., 2008):

$$\frac{d\rho}{d\varepsilon} = \frac{1}{b\lambda} - f\rho = \frac{1}{b}\left(\frac{1}{D} + \frac{1}{D_t} + k\sqrt{\rho}\right) - f\rho, \tag{3}$$

where $f$ is a rate- and temperature-dependent dynamic-recovery coefficient, $k$ is a constant that characterizes dislocation storage due to dislocation interactions, and $D_t$ is the twin spacing. In this model, changes in the dislocation mean free path are sensitive to the total dislocation density, grain size and twin spacing. An additional term, given by the product of the recovery factor and the dislocation density, $f\rho$, is subtracted to account for dynamic recovery processes. Rybacki et al. (2021) argued that this model could potentially capture the rheological behavior of calcite polycrystals.

The dynamic Hall-Petch model of Bouaziz et al. (2008) provides a physical basis for the dependence of stress on the square root of twin density at low stress. Rybacki et al. (2021) also argued that the high hardening rates (3%–5% of the shear modulus, Figure 5) observed in calcite rocks are also consistent with TWIP. However, it should be noted that high hardening rates (compared to typical expectations in metals of 0.5%–1% of the shear modulus) are not unique to calcite rocks as olivine, which does not twin, exhibits hardening rates up to 5%–10% of the shear modulus when deformed by low-temperature plasticity (Druiventak et al., 2011; Hansen et al., 2019).

The TWIP model also suggests that the hardening rate should be dominated by twin spacing as $D_t$ is always at least 1–2 orders of magnitude smaller than the grain size $D$ (Figure 14). Taking the case of Carrara marble at 600 MPa, 200°C with $D$ = 100 μm and $D_t$ = 5 μm, we might expect strain hardening of $450\alpha\mu$ (neglecting recovery and forest hardening). At the same conditions for Wombeyan marble, $D$ = 1 mm and $D_t$ = 7.5 μm, so that strain hardening should be of $360\alpha\mu$. The ratio of hardening rates would therefore be 1.25. The actual hardening rates observed in our experiments are in a ratio of 2 (considering $H_5$ = 1.6 and 0.8 GPa for Carrara marble and Wombeyan marble respectively), which suggests that twins may have a smaller impact on hardening than anticipated from Equation 3.

#### 4.3.1. Twins as Potential Barriers to Dislocations

Our main observation is that of strengthening with decreasing grain size (Figure 4), and it is difficult to assess the exact role of twins in the hardening behavior from our macroscopic data alone. The TWIP model is founded on the notion that twins produce further hardening by either retarding or stopping dislocation motion. In order to test the potential validity of the TWIP model in calcite, in this Section we assess the respective efficiency of grain boundaries and twins at impeding dislocations.

Microstructural observations suggest that the interaction between dislocations and twins boundaries varies between grains. Some grains contain lattice curvature that is clearly affected by twin boundaries (e.g., Figure 12c) whereas in other grains the lattice curvature appears to be unaffected by twin boundaries (e.g., Figures 9c and 12d). There are a number of factors that could explain these observations, including elastic anisotropy, the relative orientation of each grain with respect to loading (e.g., different Schmid factors for dominant slip systems), and the interrelation between slip-plane and twin-plane orientations that could lead to different potential for twins to stop dislocations.

We can assess the effectiveness of twin boundaries and grain boundaries as barriers to dislocations by considering slip-transmission coefficients. The simplest form of this analysis is purely geometric and considers only the slip-plane orientation and direction of the Burgers vector of the incoming and outgoing slip systems (Luster & Morris, 1995),

$$m' = (n_A \cdot n_B)(b_A \cdot b_B) = \cos(\phi)\cos(\kappa) \tag{4}$$

where $n$ denotes the unit normal vector of the slip plane and $b$ the unit Burgers vector, and the subscripts A and B denote the incoming and outgoing slip systems. A value of zero for $m'$ indicates an impenetrable barrier to dislocations and a value of one indicates a transparent boundary.

Extensive work by J. De Bresser and Spiers (1990), J. H. P. De Bresser and Spiers (1993), and J. H. De Bresser and Spiers (1997) demonstrated that $r\{10\bar{1}4\}\langle\bar{2}021\rangle^{\pm}$ and $f\{\bar{1}012\}\langle 2\bar{2}01\rangle^{\pm}$ are the dominant slip systems in calcite at low temperatures. The critical resolved shear stresses of these slip systems is about an order of magnitude greater than that of $e$ twinning at room temperature. Despite their strength, we consider them to be active in our samples since our stress level is typically significantly above this level and we observe significant intragranular misorientation. For each twin system $e_1$, $e_2$, and $e_3$, we computed the maximum value of $m'$ amongst the possible $r$ and $f$ slip systems across the twin boundary (Table 7). We find that $m'$ is always greater than 0.4, and in some cases twins are transparent with a value of 1 (e.g., $r_2^+$ to $r_3^+$ across an $e_1$ twin). This analysis suggests that twin boundaries are less likely, on average, to impede dislocation motion compared to randomly oriented grain boundaries.

To further test this result, we computed the expected $m'$ values for our EBSD data across the activated twin systems within each grain (Figure 16). The results demonstrate that grains with low values of $m'$ (Figure 16, grain c) exhibit dislocation substructures that are affected by twinning, that is segmentation of lattice distortion between twins (Figure 12c). In contrast, grains with large values of $m'$ (Figure 16, grain d) exhibit gradients in lattice distortion over length scales approaching the grain size, but which are not strongly affected at smaller scales by twin boundaries. HR-EBSD maps taken from the interior of these grains supports this conclusion, large residual stresses and GND densities are observed in the vicinity of twin boundaries in grains for which $m'$ is small (Figures 13b and 13c). Lower residual stresses and GND densities are present in the vicinity of twin boundaries in grains for which $m'$ is low (Figures 13a and 16b). The efficacy of twin boundaries as barriers to dislocation motion is therefore dependent on the local orientation of individual grains, but is on average weaker than a grain boundary taken at random.

To further compare the effect of twin and grain boundaries on dislocation motion, another, complementary geometric criterion can be used that quantifies the degree of misalignment between the line intersections of incoming and outgoing slip planes with a grain or twin boundary, $\mathbf{l}_A$ and $\mathbf{l}_B$, respectively, and between their slip directions, $\mathbf{d}_A$ and $\mathbf{d}_B$, respectively. The following scalar quantity is maximal when the two slip systems on either side of the boundary are aligned and slip can be transmitted easily across the boundary (Bayerschen et al., 2016; Shen et al., 1986):

$$\hat{M} = (\mathbf{l}_A \cdot \mathbf{l}_B)(\mathbf{d}_A \cdot \mathbf{d}_B). \tag{5}$$

**Table 7**
*Slip-Transmission Analysis of Twin Boundaries*

| $S_A$ | Maximum $m'_{e1}$ | $S_B$ | Maximum $m'_{e2}$ | $S_B$ | Maximum $m'_{e3}$ | $S_B$ |
|---|---|---|---|---|---|---|
| $r_1^-$ | 0.617 | $r_1^-$ | 0.414 | $f_1\langle\bar{2}20\bar{1}\rangle^-$ | 0.414 | $f_2\langle20\bar{2}\bar{1}\rangle^-$ |
| $r_2^-$ | 0.414 | $f_2\langle20\bar{2}\bar{1}\rangle^-$ | 0.617 | $r_2^-$ | 0.414 | $f_2\langle0\bar{2}2\bar{1}\rangle^-$ |
| $r_3^-$ | 0.414 | $f_3\langle20\bar{2}\bar{1}\rangle^-$ | 0.414 | $f_3\langle\bar{2}20\bar{1}\rangle^-$ | 0.617 | $r_3^-$ |
| $r_1^+$ | 0.630 | $r_1^+$ | 1.000 | $r_3^+$ | 1.000 | $r_2^+$ |
| $r_2^+$ | 1.000 | $r_3^+$ | 0.630 | $r_2^+$ | 1.000 | $r_1^+$ |
| $r_3^+$ | 1.000 | $r_2^+$ | 1.000 | $r_1^+$ | 0.630 | $r_3^+$ |
| $f_1\langle\bar{2}20\bar{1}\rangle^-$ | 0.541 | $r_1^-$ | 0.718 | $f_1\langle\bar{2}20\bar{1}\rangle^-$ | 0.596 | $f_1\langle0\bar{2}2\bar{1}\rangle^-$ |
| $f_1\langle2\bar{2}01\rangle^+$ | 0.541 | $r_1^-$ | 0.718 | $f_1\langle\bar{2}20\bar{1}\rangle^-$ | 0.596 | $f_1\langle0\bar{2}2\bar{1}\rangle^-$ |
| $f_2\langle0\bar{2}2\bar{1}\rangle^-$ | 0.596 | $f_2\langle20\bar{2}\bar{1}\rangle^-$ | 0.541 | $r_2^-$ | 0.718 | $f_2\langle0\bar{2}2\bar{1}\rangle^-$ |
| $f_2\langle02\bar{2}1\rangle^+$ | 0.596 | $f_2\langle20\bar{2}\bar{1}\rangle^-$ | 0.541 | $r_2^-$ | 0.718 | $f_2\langle0\bar{2}2\bar{1}\rangle^-$ |
| $f_3\langle20\bar{2}\bar{1}\rangle^-$ | 0.718 | $f_3\langle20\bar{2}\bar{1}\rangle^-$ | 0.596 | $f_3\langle\bar{2}20\bar{1}\rangle^-$ | 0.541 | $r_3^-$ |
| $f_3\langle\bar{2}021\rangle^+$ | 0.718 | $f_3\langle20\bar{2}\bar{1}\rangle^-$ | 0.596 | $f_3\langle\bar{2}20\bar{1}\rangle^-$ | 0.541 | $r_3^-$ |
| $f_1\langle0\bar{2}2\bar{1}\rangle^-$ | 0.541 | $r_1^-$ | 0.596 | $f_1\langle\bar{2}20\bar{1}\rangle^-$ | 0.717 | $f_1\langle0\bar{2}2\bar{1}\rangle^-$ |
| $f_1\langle02\bar{2}1\rangle^+$ | 0.541 | $r_1^-$ | 0.596 | $f_1\langle\bar{2}20\bar{1}\rangle^-$ | 0.717 | $f_1\langle0\bar{2}2\bar{1}\rangle^-$ |
| $f_2\langle20\bar{2}\bar{1}\rangle^-$ | 0.596 | $f_2\langle20\bar{2}\bar{1}\rangle^-$ | 0.541 | $r_2^-$ | 0.596 | $f_2\langle0\bar{2}2\bar{1}\rangle^-$ |
| $f_2\langle\bar{2}021\rangle^+$ | 0.596 | $f_2\langle20\bar{2}\bar{1}\rangle^-$ | 0.541 | $r_2^-$ | 0.596 | $f_2\langle0\bar{2}2\bar{1}\rangle^-$ |
| $f_3\langle\bar{2}20\bar{1}\rangle^-$ | 0.718 | $f_3\langle20\bar{2}\bar{1}\rangle^-$ | 0.718 | $f_3\langle\bar{2}20\bar{1}\rangle^-$ | 0.541 | $r_3^-$ |
| $f_3\langle2\bar{2}01\rangle^+$ | 0.718 | $f_3\langle20\bar{2}\bar{1}\rangle^-$ | 0.718 | $f_3\langle\bar{2}20\bar{1}\rangle^-$ | 0.541 | $r_3^-$ |

*Note.* Tabulated results for the maximum value of $m'$ (Equation 4) between slip system $S_A$ and $S_B$. The $m'$ subscript denotes the twinning system considered: for example, $m'_{e1}$ represents slip transfer across an $e1$ twin.

The line intersections $\mathbf{l}$ can be obtained from $\mathbf{l} = (\mathbf{n} \times \mathbf{n}_\Gamma)/|\mathbf{n}_A \times \mathbf{n}_\Gamma|$, where $\mathbf{n}_\Gamma$ is the twin boundary plane normal.

We used the $\hat{M}$ criterion to compare the efficiency of slip transmission across twin boundaries to slip transmission across grain boundaries. A random fabric was generated using MTEX, and we computed $\hat{M}$ between random grain pairs by assuming that the activated slip system (either $r^\pm$ or $f^\pm$ slip) was that with highest Schmid factor in each grain (assuming uniaxial compression). For each grain, we also computed $\hat{M}$ across a twin boundary hosted in the initial grain, the activated twin system was assumed to be that with the highest Schmid factor in each grain. These calculations suggest an average value for slip transmission of $\hat{M} = 0.27$ across grain boundaries, which is considerably smaller than the average value of $\hat{M} = 0.43$ for slip transfer across twin boundaries (Figure 17).

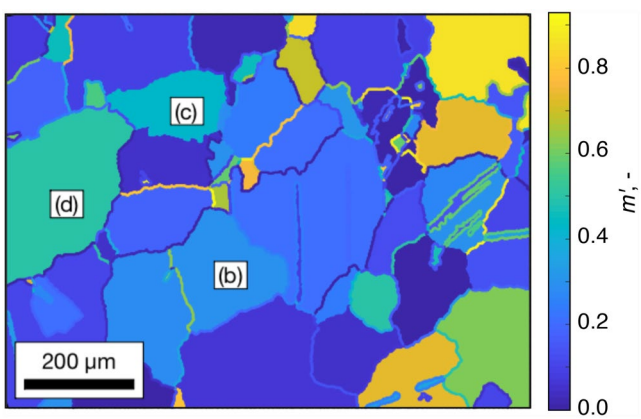


**Figure 16.** Map of $m'$ values for slip transmission across grain boundaries (colored according to value) and twin boundaries (grains colored according to value) computed from electron backscatter diffraction data obtained for Run0093 ($P = 600$ MPa, $T = 200$°C). The labels (b–d) refer to the inset figures in Figure 12.

The relative ease with which dislocations can transmit across twin boundaries suggests that Equation 3 requires refinement. We suggest that weights should be applied to the contributions of twin boundaries and grain boundaries, such that Equation 3 becomes,

$$\frac{d\rho}{d\varepsilon} = \frac{1}{b\lambda} - f\rho = \frac{1}{b}\left(\frac{k_D}{D} + \frac{k_t}{D_t} + k\sqrt{\rho}\right) - f\rho, \quad (6)$$

in which $k_D$ and $k_t$ are weights to account for the relative efficacy of grain boundaries and twin boundaries. Note that the coefficient for grain size $k_D$ is distinct from the Hall-Petch coefficient $K$. We expect that $k_t \ll k_D$. Further microstructural measurements, such as the evolution of twin density with strain, are required to determine the value of these weighting factors.

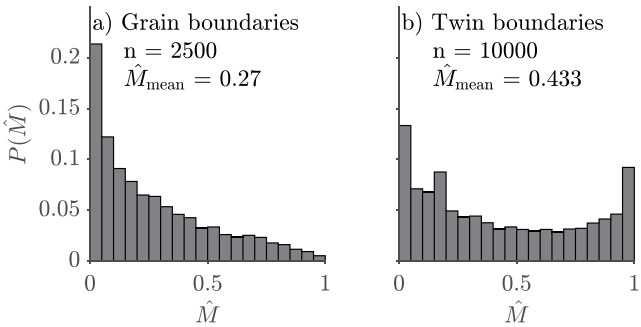


**Figure 17.** Computed values of the maximum value of $\hat{M}$ for slip systems with the largest Schmidt factor on each side a grain or twin boundary, for randomly oriented grain boundaries (a) and twin boundaries within each randomly oriented grain (b).

### 4.4. Toward a Model of Semi-Brittle Flow in Calcite Rocks

Our observations combined with previous results suggest several key characteristics that should be captured by a model of semi-brittle flow in calcite-rich rocks at $T < 400$°C: (a) non-linearly increasing strength and hardening with increasing pressure, (b) decreasing strength with increasing temperature, (c) increasing strength with decreasing grain size, (d) strength that is nearly insensitive to strain rate. Rybacki et al. (2021) reviewed proposed models of semi-brittle flow, identifying difficulties in combining brittle and plastic flow into a simple unified model.

Through the semi-brittle flow regime, the strain contribution of brittle and crystal-plastic processes changes with depth. At low pressures and temperatures, at which brittle processes dominate, the macroscopic behavior of rocks is described by frictional failure (Brace & Kohlstedt, 1980; Byerlee & Brace, 1966). Microphysical models of brittle deformation in low porosity rocks are typically based on the wing-crack model (e.g., Ashby & Sammis, 1990; Nemat-Nasser & Horii, 1982), in which brittle damage is accounted for by the propagation of Mode I wing cracks. In this regime, strength is pressure sensitive, dependent on grain size and is to first order strain rate-insensitive. There is no strong temperature dependence, and plasticity is not considered.

There are only a small number of microphysical models in existence accounting for coupled brittle-plastic deformation. Horii and Nemat-Nasser (1986) modified and solved the problem of a wing crack coupled a "plastic zone" by considering a dislocation pile-up ahead of the shear crack. Their model is sensitive to pressure, grain size and also temperature as the plastic yield strength in the plastic zone can vary with temperature. However, their model predicts that materials with coarser grain size are more brittle, contradicting observations from experimental data (Fredrich et al., 1990).

More recently, Nicolas et al. (2017) derived a model incorporating the propagation of wing cracks, plastic pore collapse and nucleation of new cracks due to dislocation pile-ups. The model reproduces several important characteristics of the deformation of porous limestones. As pointed out by Rybacki et al. (2021), this model does not consider dynamic recovery or twinning, which are important deformation processes in calcite-rich rocks. The large number of free parameters make this model challenging to test and may limit its general application.

An alternative approach to introduce feedbacks between cracking and plastic flow may be by use of a modified Kocks-Mecking equation. The anticorrelation between strain hardening and crack density observed in calcite by Fredrich et al. (1989) and confirmed by our results (Figure 15) suggests that cracking acts to reduce stress and hardening. The role of cracks could be multiple. One possibility is that strength remains dictated by dislocation density, and correctly predicted by the Taylor Equation 2, in which case a decreasing flow stress would imply a reduction of dislocation density and thus that and cracks could act as dislocation sinks. This possibility is compatible with the idea that tensile cracks correspond to free surfaces within the material, and dislocations intersecting those free surfaces would form steps and disappear from the crystals. One other possibility is that cracks relax internal stress and strain incompatibilities between grains, that is, act as "geometrically necessary" structures. A third option is that deformation at low pressure, at which cracks are pervasive, is not controlled by dislocation motion but dominated by elastically-accommodated intergranular slip, and tensile cracks relax the associated internal stresses.

The origin of microcracks during semi-brittle deformation of calcite is potentially coupled to intracrystalline plasticity. As discussed extensively by Nicolas et al. (2017), cracks can be nucleated due to stress concentrations at the head of dislocation pile-ups (e.g., Olsson & Peng, 1976; Stroh, 1954; Wong, 1990) and may therefore be dislocation sinks, that is, microcracks could contribute to dislocation escape from the deformed crystals. Where slip transfer is inefficient (Olsson & Peng, 1976) and also where geometry results in a high density of GNDs (e.g., Figure 8d) stresses are high, which can lead to the nucleation of cracks.

An approach based on the Kocks-Mecking model has the advantage that twinning and grain size effects can be incorporated, whilst introducing a confining-pressure dependence due to the propagation of Mode I cracks. At this stage however, there are insufficient data on dislocation-density evolution during semi-brittle deformation

to make sensible progress beyond the qualitative statements listed above. Thus, detailed modeling attempts are beyond the scope of the present work.

## 5. Conclusions

We performed a series of triaxial deformation experiments using three calcite rocks of variable grain size: Solnhofen limestone, Carrara marble and Wombeyan marble. Our experimental results demonstrate that the strength and hardening rates of calcite rocks deformed in the semi-brittle regime are inversely dependent on grain size, in agreement with previous work (e.g., Fredrich et al., 1990; Olsson, 1974).

Deformation tests were accompanied by in situ measurements of *P*-wave speed, which generally decreases with strain. Wave speed decreases more at room temperature than at 200 and 400°C, which is consistent with microcracking being more prevalent at low temperature.

In agreement with previous work (Fredrich et al., 1989), quantitative microstructural observations show that microcrack density is inversely proportional to hardening rate. While the exact role of cracks in the overall stress-strain behavior remains unclear at this stage, we propose the hypothesis that tensile microcracks cause weakening by either relaxing internal stresses (accommodating strain incompatibilities and reducing the need for GNDs), or offering free surfaces where dislocations can escape individual grains, or a combination thereof.

Furthermore, significant decreases in wave speed are observed upon removal of confining pressure, indicating the accumulation of sample damage. Decompression induced wave-speed decreases are greatest in experiments performed at high pressure (600 MPa) and low temperature (room temperature) in conjunction with the highest hardening rates. Microstructural observations from samples deformed at these conditions show open grain boundaries, suggesting that wave-speed decreases during decompression originate from the release of stored elastic strain.

Electron microscopy shows that twin density is high, consistent with previous studies at similar conditions. Twin spacing is always at least one order of magnitude smaller than grain size. The spatial distributions of intragranular misorientation suggest that twin boundaries do not always act as significant barriers to dislocation motion and slip-transfer computations indicate that twins are statistically weaker barriers than grain boundaries. Therefore, grain size exerts a first-order control on strength and strain hardening, whereas the spacing of twin boundaries may exert a second-order control on these properties.

Taken together, our results show that semi-brittle flow in calcite is controlled by grain-size dependent processes that lead to significant hardening. This behavior is qualitatively consistent with rheological models that include dislocation density and twin spacing as key state variables. The role of cracking in the decrease of strain hardening at low pressure and temperature requires the addition of a quantity describing crack density (that should include information on crack spacing, length, and orientation distribution) as a new state variable, to address fully the stress-strain behavior of rocks in the semi-brittle regime.

## Data Availability Statement

Processed experimental data (stress, strain, and velocity change) is available from Zenodo (https://doi.org/10.5281/zenodo.7347236).

**Acknowledgments**
Extensive discussions with Erik Rybacki and Brian Evans, who shared some of their (then) unpublished data, helped to shape this work. Emmanuel David contributed to early technical developments on the Murrell apparatus. Technical support from John Bowles and Neil Hughes is greatly appreciated. Ian Jackson kindly provided the Wombeyan marble. Sarah Incel facilitated thin section preparation. Sheng Fan helped running SEM sessions. Discussions with Thomas Breithaupt, Jörg Renner, and Chris Spiers contributed to our understanding of plastic deformation in calcite. Review comments by Brian Evans and Ian Jackson were very helpful in clarifying the manuscript. This project has received funding from the European Research Council (ERC) under the European Union's Horizon 2020 research and innovation programme (grant agreement 804685/"RockDEaF" to N.B.) and from the UK Natural Environment Research Council (Grant Agreement NE/M016471/1 to N.B.). DW acknowledges support from a UK Research and Innovation Future Leaders Fellowship (Grant Agreement MR/V021788/1).

## References

Ashby, M. (1970). The deformation of plastically non-homogeneous materials. *Philosophical Magazine*, *21*(170), 37–41. https://doi.org/10.1080/14786437008238426

Ashby, M., & Sammis, C. (1990). The damage mechanics of brittle solids in compression. *Pure and Applied Geophysics*, *133*(3), 489–521. https://doi.org/10.1007/bf00878002

Barber, D. J., & Wenk, H. R. (1979). Deformation twinning in calcite, dolomite, and other rhombohedral carbonates. *Physics and Chemistry of Minerals*, *5*(2), 141–165. https://doi.org/10.1007/BF00307550

Baud, P., Schubnel, A., & Wong, T.-F. (2000). Dilatancy, compaction, and failure mode in Solnhofen limestone. *Journal of Geophysical Research*, *105*(B8), 289–303. https://doi.org/10.1029/2000jb900133

Bayerschen, E., McBride, A. T., Reddy, B. D., & Böhlke, T. (2016). Review on slip transmission criteria in experiments and crystal plasticity models. *Journal of Materials Science*, *51*(5), 2243–2258. https://doi.org/10.1007/s10853-015-9553-4

Birch, F. (1961). The velocity of compressional waves in rocks to 10 kilobars, part 2. *Elastic Properties and Equations of State*, *66*, 2199–2224. https://doi.org/10.1029/SP026p0091

Bouaziz, O., Allain, S., & Scott, C. (2008). Effect of grain and twin boundaries on the hardening mechanisms of twinning-induced plasticity steels. *Scripta Materialia*, *58*(6), 484–487. https://doi.org/10.1016/j.scriptamat.2007.10.050

Brace, W. F., & Kohlstedt, D. L. (1980). Limits on lithospheric stress imposed by laboratory experiments. *Journal of Geophysical Research: Solid Earth*, *85*(B11), 6248–6252. https://doi.org/10.1029/jb085ib11p06248

Britton, T. B., & Wilkinson, A. J. (2011). Measurement of residual elastic strain and lattice rotations with high resolution electron backscatter diffraction. *Ultramicroscopy*, *111*(8), 1395–1404. https://doi.org/10.1016/j.ultramic.2011.05.007

Britton, T. B., & Wilkinson, A. J. (2012). High resolution electron backscatter diffraction measurements of elastic strain variations in the presence of larger lattice rotations. *Ultramicroscopy*, *114*, 82–95. https://doi.org/10.1016/j.ultramic.2012.01.004

Burov, E. B. (2011). Rheology and strength of the lithosphere. *Marine and Petroleum Geology*, *28*(8), 1402–1443. https://doi.org/10.1016/j.marpetgeo.2011.05.008

Byerlee, J. D., & Brace, W. F. (1966). Stick-slip as a mechanism for earthquakes. *Science*, *153*(3739), 990–992. https://doi.org/10.1126/science.153.3739.990

Conrad, H., Feuerstein, S., & Rice, L. (1967). Effects of grain size on the dislocation density and flow stress of niobium. *Materials Science and Engineering*, *2*(3), 157–168. https://doi.org/10.1016/0025-5416(67)90032-8

Cordero, Z. C., Knight, B. E., & Schuh, C. A. (2016). Six decades of the Hall–Petch effect—A survey of grain-size strengthening studies on pure metals. *International Materials Reviews*, *61*(8), 495–512. https://doi.org/10.1080/09506608.2016.1191808

David, E. C., Brantut, N., & Hirth, G. (2020). Sliding crack model for nonlinearity and hysteresis in the triaxial stress-strain curve of rock, and application to antigorite deformation. *Journal of Geophysical Research: Solid Earth*, *125*(10), 1–35. https://doi.org/10.1029/2019JB018970

De Bresser, J., & Spiers, C. J. (1990). High-temperature deformation of calcite single crystals by r+ and f+ slip. *Geological Society Special Publications*, *54*(54), 285–298. https://doi.org/10.1144/GSL.SP.1990.054.01.25

De Bresser, J. H. (1991). *Intracrystalline deformation of calcite* (Doctoral dissertation). Utrecht University. Retrieved from https://dspace.library.uu.nl/handle/1874/237314

De Bresser, J. H., & Spiers, C. J. (1997). Strength characteristics of the r, f, and c slip systems in calcite. *Tectonophysics*, *272*(1), 1–23. https://doi.org/10.1016/S0040-1951(96)00273-9

De Bresser, J. H. P. (1996). Steady state dislocation densities in experimentally deformed calcite materials: Single crystals versus polycrystals. *Journal of Geophysical Research: Solid Earth*, *101*(B10), 22189–22201. https://doi.org/10.1029/96jb01759

De Bresser, J. H. P., & Spiers, C. J. (1993). Slip systems in calcite single crystals deformed at 300–800°C. *Journal of Geophysical Research: Solid Earth*, *98*(B4), 6397–6409. https://doi.org/10.1029/92jb02044

De Cooman, B. C., Estrin, Y., & Kim, S. K. (2018). Twinning-induced plasticity (TWIP) steels. *Acta Materialia*, *142*, 283–362. https://doi.org/10.1016/j.actamat.2017.06.046

Donath, F. A., & Fruth, L. S. (1971). Dependence of strain-rate effects on deformation mechanism and rock type. *The Journal of Geology*, *79*(3), 347–371. https://doi.org/10.1086/627630

Druiventak, A., Trepmann, C. A., Renner, J., & Hanke, K. (2011). Low-temperature plasticity of olivine during high stress deformation of peridotite at lithospheric conditions—An experimental study. *Earth and Planetary Science Letters*, *311*(3–4), 199–211. https://doi.org/10.1016/j.epsl.2011.09.022

Dunstan, D. J., & Bushby, A. J. (2014). Grain size dependence of the strength of metals: The Hall-Petch effect does not scale as the inverse square root of grain size. *International Journal of Plasticity*, *53*, 56–65. https://doi.org/10.1016/j.ijplas.2013.07.004

Edmond, J. M., & Paterson, M. S. (1972). Volume changes during the deformation of rocks at high pressures. *International Journal of Rock Mechanics and Mining Sciences*, *9*(2), 161–182. https://doi.org/10.1016/0148-9062(72)90019-8

Evans, B., & Kohlstedt, D. L. (1995). Rheology of rocks. In T. Ahrens (Ed.), *Rock physics phase relations* (pp. 148–165). American Geophysical Union (AGU). https://doi.org/10.1029/RF003p0148

Fischer, G., & Paterson, M. S. (1989). Dilatancy during rock deformation at high temperatures and pressures. *Journal of Geophysical Research*, *94*(B12), 607–617. https://doi.org/10.1007/978-3-540-29678-25364

Fredrich, J. T., Evans, B., & Wong, T. F. (1989). Micromechanics of the brittle to plastic transition in Carrara marble. *Journal of Geophysical Research*, *94*(B4), 4129–4145. https://doi.org/10.1029/JB094iB04p04129

Fredrich, J. T., Evans, B., & Wong, T.-F. (1990). Effect of grain size on brittle and semibrittle strength: Implications for micromechanical modelling of failure in compression. *Journal of Geophysical Research*, *95*(B7), 10907. https://doi.org/10.1029/jb095ib07p10907

French, M. E., Zhu, W., Xiao, X., Evans, B., & Prior, D. J. (2022). Thermally enhanced water weakening of the Solnhofen limestone. *Journal of Geophysical Research: Solid Earth*, *127*(3), e2021JB022742. https://doi.org/10.1029/2021jb022742

Goetze, C., & Brace, W. F. (1972). Laboratory observations of high-temperature rheology of rocks. *Tectonophysics*, *13*(1–4), 583–600. https://doi.org/10.1016/0040-1951(72)90039-X

Goetze, C., & Evans, B. (1979). Stress and temperature in the bending lithosphere as constrained by experimental rock mechanics. *Geophysical Journal of the Royal Astronomical Society*, *59*(3), 463–478. https://doi.org/10.1111/j.1365-246X.1979.tb02567.x

Groma, I., & Bakó, B. (1998). Probability distribution of internal stresses in parallel straight dislocation systems. *Physical Review B: Condensed Matter and Materials Physics*, *58*(6), 2969–2974. https://doi.org/10.1103/PhysRevB.58.2969

Hall, E. O. (1951). The deformation and ageing of mild steel: III discussion of results. *Proceedings of the Physical Society Section B*, *64*(9), 747–753. https://doi.org/10.1088/0370-1301/64/9/303

Hansen, L. N., Kumamoto, K. M., Thom, C. A., Wallis, D., Durham, W. B., Goldsby, D. L., et al. (2019). Low-temperature plasticity in olivine: Grain size, strain hardening, and the strength of the lithosphere. *Journal of Geophysical Research: Solid Earth*, *124*(6), 5427–5449. https://doi.org/10.1029/2018JB016736

Harbord, C., Brantut, N., David, E. C., & Mitchell, T. M. (2022). A high pressure, high temperature gas medium apparatus to measure acoustic velocities during deformation of rock. *Review of Scientific Instruments*, *93*(5), 053908. https://doi.org/10.1063/5.0084477

Heard, H. C. (1960). Chapter 7: Transition from brittle fracture to ductile flow in Solenhofen limestone as a function of temperature, confining pressure, and interstitial fluid pressure. In *Memoir of the Geological Society of America* (Vol. 1933, pp. 193–226). https://doi.org/10.1130/MEM79-p193

Horii, H., & Nemat-Nasser, N. (1986). Brittle failure in compression: Splitting faulting and brittle-ductile transition. *Philosophical Transactions of the Royal Society of London. Series A, Mathematical and Physical Sciences*, *319*(1549), 337–374. https://doi.org/10.1098/rsta.1986.0101

Jamison, W. R., & Spang, J. H. (1976). Use of calcite twin lamellae to infer differential stress. *Bulletin of the Geological Society of America*, *87*(6), 868–872. https://doi.org/10.1130/0016-7606(1976)87⟨868:UOCTLT⟩2.0.CO;2

Jiang, J., Britton, T. B., & Wilkinson, A. J. (2013). Evolution of dislocation density distributions in copper during tensile deformation. *Acta Materialia*, *61*(19), 7227–7239. https://doi.org/10.1016/j.actamat.2013.08.027

Kalácska, S., Groma, I., Borbély, A., & Ispánovity, P. D. (2017). Comparison of the dislocation density obtained by HR-EBSD and X-ray profile analysis. *Applied Physics Letters*, *110*(9), 91912. https://doi.org/10.1063/1.4977569

Kocks, U. F. (1966). A statistical theory of flow stress and work-hardening. *Philosophical Magazine*, *13*(123), 541–566. https://doi.org/10.1080/14786436608212647

Kocks, U. F. (1976). Laws for work-hardening and low-temperature creep. *Journal of Engineering Materials and Technology*, *98*(1), 76–85. https://doi.org/10.1115/1.3443340

Li, J. C. (1963). Petch relation and grain boundary sources. *Transactions of the Metallurgical Society of AIME*, *227*(1), 239.

Li, Y., Bushby, A. J., & Dunstan, D. J. (2016). The Hall-Petch effect as a manifestation of the general size effect. *Proceedings of the Royal Society A: Mathematical, Physical and Engineering Sciences*, *472*, 2190. https://doi.org/10.1098/rspa.2015.0890

Luster, J., & Morris, M. A. (1995). Compatibility of deformation in two-phase Ti-Al alloys: Dependence on microstructure and orientation relationships. *Metallurgical and Materials Transactions A: Physical Metallurgy and Materials Science*, *26*(7), 1745–1756. https://doi.org/10.1007/BF02670762

Maurice, C., Dzieciol, K., & Fortunier, R. (2011). A method for accurate localisation of EBSD pattern centres. *Ultramicroscopy*, *111*(2), 140–148. https://doi.org/10.1016/j.ultramic.2010.10.007

Mecking, H., & Kocks, U. F. (1981). Kinetics of flow and strain-hardening. *Acta Metallurgica*, *29*(11), 1865–1875. https://doi.org/10.1016/0001-6160(81)90112-7

Meyer, G. G., Brantut, N., Mitchell, T. M., Meredith, P. G., & Plümper, O. (2021). Time dependent mechanical crack closure as a potential rapid source of post-seismic wave speed recovery: Insights from experiments in Carrara marble. *Journal of Geophysical Research: Solid Earth*, *126*(4), 1–29. https://doi.org/10.1029/2020JB021301

Meyers, M. A., & Ashworth, E. (1982). A model for the effect of grain size on the yield stress of metals. *Philosophical Magazine A*, *46*(5), 737–759. https://doi.org/10.1080/01418618208236928

Mikami, Y., Oda, K., Kamaya, M., & Mochizuki, M. (2015). Effect of reference point selection on microscopic stress measurement using EBSD. *Materials Science and Engineering A*, *647*, 256–264. https://doi.org/10.1016/j.msea.2015.09.004

Mogi, K. (1964). Deformation and fracture of rocks under confining pressure (1) compression tests on dry rock sample. *Bulletin of the Earthquake Research Institute*, *42*(3), 491–514.

Nemat-Nasser, S., & Horii, H. (1982). Compression-induced nonplanar crack extension with application to splitting, exfoliation, and rockburst. *Journal of Geophysical Research*, *87*(B8), 6805–6821. https://doi.org/10.1029/JB087iB08p06805

Nicolas, A., Fortin, J., & Guéguen, Y. (2017). Micromechanical constitutive model for low-temperature constant strain rate deformation of limestones in the brittle and semi-brittle regime. *Geophysical Journal International*, *211*(1), 300–321. https://doi.org/10.1093/GJI/GGX299

Olsson, W. A. (1974). Grain size dependence of yield stress in marble. *Journal of Geophysical Research*, *79*(32), 4859–4862. https://doi.org/10.1029/jb079i032p04859

Olsson, W. A., & Peng, S. S. (1976). Microcrack nucleation in marble. *International Journal of Rock Mechanics and Mining Sciences & Geomechanics*, *13*(2), 53–59. https://doi.org/10.1016/0148-9062(76)90704-X

Paterson, M. S. (1958). Experimental deformation and faulting in wombeyan marble. *Bulletin of the Geological Society of America*, *69*(4), 465–476. https://doi.org/10.1130/0016-7606(1958)69[465:EDAFIW]2.0.CO;2

Petch, N. J. (1953). The cleavage strength of polycrystals. *Journal of the Iron and Steel Institute*, *174*, 25–28.

Prior, D. J., Trimby, P. W., Weber, U. D., & Dingley, D. J. (1996). Orientation contrast imaging of microstructures in rocks using forescatter detectors in the scanning electron microscope. *Mineralogical Magazine*, *60*(403), 859–869. https://doi.org/10.1180/minmag.1996.060.403.01

Quintanilla-Terminel, A., & Evans, B. (2016). Heterogeneity of inelastic strain during creep of Carrara marble: Microscale strain measurement technique. *Journal of Geophysical Research: Solid Earth*, *121*(8), 5736–5760. https://doi.org/10.1002/2016JB012970

Quintanilla-Terminel, A., Zimmerman, M. E., Evans, B., & Kohlstedt, D. L. (2017). Microscale and nanoscale strain mapping techniques applied to creep of rocks. *Solid Earth*, *8*(4), 751–765. https://doi.org/10.5194/se-8-751-2017

Renner, J., Evans, B., & Siddiqi, G. (2002). Dislocation creep of calcite. *Journal of Geophysical Research: Solid Earth*, *107*(B12), ECV6-1–ECV6-16. https://doi.org/10.1029/2001jb001680

Rowe, K. J., & Rutter, E. H. (1990). Palaeostress estimation using calcite twinning: Experimental calibration and application to nature. *Journal of Structural Geology*, *12*(1), 1–17. https://doi.org/10.1016/0191-8141(90)90044-Y

Rutter, E. H. (1974). The influence of temperature, strain rate and interstitial water in the experimental deformation of calcite rocks. *Tectonophysics*, *22*(3–4), 311–334. https://doi.org/10.1016/0040-1951(74)90089-4

Rutter, E. H. (1986). On the nomenclature of mode of failure transitions in rocks. *Tectonophysics*, *122*(3–4), 381–387. https://doi.org/10.1016/0040-1951(86)90153-8

Rutter, E. H., Wallis, D., & Kosiorek, K. (2022). Application of electron backscatter diffraction to calcite-twinning paleopiezometry. *Geosciences*, *12*(6), 222. https://doi.org/10.3390/geosciences12060222

Rybacki, E., Evans, B., Janssen, C., Wirth, R., & Dresen, G. (2013). Influence of stress, temperature, and strain on calcite twins constrained by deformation experiments. *Tectonophysics*, *601*, 20–36. https://doi.org/10.1016/j.tecto.2013.04.021

Rybacki, E., Niu, L., & Evans, B. (2021). Semi-brittle deformation of Carrara marble: Hardening and twinning induced plasticity. *Journal of Geophysical Research: Solid Earth*, *126*(12), e2021JB022573. https://doi.org/10.1029/2021jb022573

Scholz, C. H. (1998). Earthquakes and friction laws. *Nature*, *391*(6662), 37–42. https://doi.org/10.1038/34097

Scholz, C. H. (2002). The mechanics of earthquakes and faulting. https://doi.org/10.1017/cbo9780511818516

Schubnel, A., Fortin, J., Burlini, L., & Guéguen, Y. (2005). Damage and recovery of calcite rocks deformed in the cataclastic regime. *Geological Society Special Publications*, *245*(1), 203–221. https://doi.org/10.1144/GSL.SP.2005.245.01.10

Shen, Z., Wagoner, R., & Clark, W. (1986). Dislocation pile-up and grain boundary interactions in 304 stainless steel. *Scripta Metallurgica*, *20*(6), 921–926. https://doi.org/10.1016/0036-9748(86)90467-9

Spiers, C. J. (1979). Fabric development in calcite polycrystals deformed at 400°C. *Bulletin de Minéralogie*, *102*(2), 282–289. https://doi.org/10.3406/bulmi.1979.7289

Stroh, A. (1954). The Formation of cracks as a result of plastic flow. *Proceedings of the Royal Society of London. Series A. Mathematical and Physical Sciences*, *223*(1154), 404–414.

Taylor, G. (1934). The mechanism of plastic deformation of crystals. Part I.—Theoretical. *Proceedings of the Royal Society of London Series A: Containing Papers of a Mathematical and Physical Character*, *145*(855), 362–387. https://doi.org/10.1098/rspa.1934.0106

Townend, J., & Zoback, M. D. (2000). How faulting keeps the crust strong. *Geology*, *28*(5), 399–402. https://doi.org/10.1130/0091-7613(2000)028⟨0399:HFKTCS⟩2.3.CO;2

Turner, F. J., Griggs, D. T., & Heard, H. C. (1954). Experimental deformation of calcite crystals. *Geological Society of America Bulletin*, *65*(9), 883–934. https://doi.org/10.1130/0016-7606(1954)65[883:edocc]2.0.co;2

Underwood, E. E. (1970). *Quantitative stereology*. Addison-Wesley Publishing Co.

Wallis, D., Hansen, L. N., Britton, T. B., & Wilkinson, A. J. (2019). High-angular resolution electron backscatter diffraction as a new tool for mapping lattice distortion in geological minerals. *Journal of Geophysical Research: Solid Earth*, *124*(7), 6337–6358. https://doi.org/10.1029/2019JB017867

Wallis, D., Hansen, L. N., Wilkinson, A. J., & Lebensohn, R. A. (2021). Dislocation interactions in olivine control postseismic creep of the upper mantle. *Nature Communications*, *12*(1), 1–12. https://doi.org/10.1038/s41467-021-23633-8

Wallis, D., Lloyd, G. E., & Hansen, L. N. (2018). The role of strain hardening in the transition from dislocation-mediated to frictional deformation of marbles within the Karakoram Fault Zone, NW India. *Journal of Structural Geology*, *107*(June 2017), 25–37. https://doi.org/10.1016/j.jsg.2017.11.008

Wallis, D., Sep, M., & Hansen, L. N. (2022). Transient creep in subduction zones by long-range dislocation interactions in olivine. *Journal of Geophysical Research: Solid Earth*, *127*(1), e2021JB022618. https://doi.org/10.1029/2021JB022618

Wilkinson, A. J., Meaden, G., & Dingley, D. J. (2006). High-resolution elastic strain measurement from electron backscatter diffraction patterns: New levels of sensitivity. *Ultramicroscopy*, *106*(4–5), 307–313. https://doi.org/10.1016/j.ultramic.2005.10.001

Wilkinson, A. J., Tarleton, E., Vilalta-Clemente, A., Jiang, J., Britton, T. B., & Collins, D. M. (2014). Measurement of probability distributions for internal stresses in dislocated crystals. *Applied Physics Letters*, *105*(18), 181907. https://doi.org/10.1063/1.4901219

Wong, T.-F. (1990). A note on the propagation behavior of a crack nucleated by a dislocation pileup. *Journal of Geophysical Research*, *95*(B6), 8639. https://doi.org/10.1029/JB095iB06p08639